European Journal of Environmental and Civil Engineering

Volume 26 Number 13 November 2022

Editors-in-chief
Günther Meschke
François Nicot

Taylor & Francis

ISSN: (Print) (Online) Journal homepage: www.tandfonline.com/journals/tece20

# Neural network-based optimization of fibres for seismic retrofitting applications of UHPFRC

Joaquín Abellán-García, Jairo A. DSánchez-Díaz & Victoria Eugenia Ospina-Becerra

**To cite this article:** Joaquín Abellán-García, Jairo A. DSánchez-Díaz & Victoria Eugenia Ospina-Becerra (2022) Neural network-based optimization of fibres for seismic retrofitting applications of UHPFRC, European Journal of Environmental and Civil Engineering, 26:13, 6305-6333, DOI: 10.1080/19648189.2021.1938687

**To link to this article:** https://doi.org/10.1080/19648189.2021.1938687

EUROPEAN JOURNAL OF ENVIRONMENTAL AND CIVIL ENGINEERING
2022, VOL. 26, NO. 13, 6305–6333
https://doi.org/10.1080/19648189.2021.1938687



# Neural network-based optimization of fibres for seismic retrofitting applications of UHPFRC

Joaquín Abellán-García[a], Jairo A. DSánchez-Díaz[b] and Victoria Eugenia Ospina-Becerra[a]

[a]Escuela Colombiana de Ingeniería Julio Garavito, Bogotá, Colombia; [b]Information Management, Escuela Colombiana de Ingeniería Julio Garavito, Bogotá, Colombia

**ABSTRACT**

Ultra-high-performance fibre reinforced concrete (UHPFRC) is an advanced construction material that provides new opportunities in the future of the construction industry around the world. Among those new applications, rehabilitation, and seismic retrofitting of existing damaged or non-ductile concrete structures can be highlighted. The main objective of this paper is to optimise the hybrid blend of fibres that allows a previously optimised eco-friendly ultra-high-performance cementitious paste to achieve the ductility requirements for seismic retrofitting applications at lower costs. To meet this goal, two artificial neural network models (ANNs) were created to predict the energy absorption capacity (g) and maximum post-cracking strain ($\varepsilon$pc). A total of 50 own experimental campaign data added to 550 published works throughout the world data were used for training purposes by using the R-code language. Once the models were trained and validated, a multi-objective optimisation was used to select the combination of fibres that achieved the limit values of $g \geq 50$ kJ/m3 and $\varepsilon pc \geq 0.3\%$ considering cost constraints. The experimentally validated results indicated that the adequate blend of high strength steel micro-fibres and hooked end normal strength steel fibres fulfil the threshold values at a lower cost.

**ARTICLE HISTORY**
Received 25 February 2021
Accepted 31 May 2021

**KEYWORDS**
UHPFRC; artificial neural networks; ductility; multi-objective optimisation; energy absorption capacity; seismic retrofitting applications

## 1. Introduction

Seismic retrofitting of existing buildings and civil works is a challenging task that demands effective, inexpensive, and feasible strategies and technologies depending on the different structural typologies (De Domenico et al., 2019). The need to carry out seismic reinforcement of structures located in high-hazard earthquake areas can appear for different reasons and circumstances. For example, the map of seismic hazard is continuously changing and evolving, prompting the current peak ground acceleration of a particular installation site, as determined by seismic regulations currently in force today, to be higher than those prescribed in the past (De Domenico et al., 2019). Besides, many concepts of modern seismic design codes as ultimate limit states and capacity design principles have been applied in seismic standards only in very recent times and were absolutely unknown when these buildings and civil works were originally constructed (Bracci et al., 1955; Dogan & Krstulovic-Opara, 2003; Parra-Montesinos & Wight, 2000). Another possible reason for seismic retrofitting can be attributed to the increase in importance of a given structure, which automatically leads to higher seismic demand (Dagenais et al., 2018).

For example, Colombia, where this paper was written, sits at the complex junction of three small tectonic plates: the Caribbean plate to the north, the Cocos plate to the west, and the Nazca plate to the

CONTACT Joaquín Abellán García joaquin.abellan-g@escuelaing.edu.co Escuela Colombiana de Ingeniería Julio Garavito, Bogotá, Colombia

southwest. All of them border the northwest corner of the giant South American plate (Abellán et al., 2020a; Garcia, 2014).

As a result of the latter, and according to data from National Statistics and NSR-10, an estimated 90% of the Colombian population lives under high or moderate seismic hazard (Garcia, 2014; Sísmica & de, 2010). Besides, since 1984 Colombia has had regulations for earthquake-resistant constructions (Garcia, 2014; Sísmica & de, 2010). Thus, buildings and civil works constructed before that date have a good chance of being considered as vulnerable, depending on their location. In addition, there is a high percentage of informal construction in the country, which also can be considered as vulnerable (Abellán et al., 2020a).

As a result of this, and according to several researches from Universidad de Los Andes and the Colombian Association of Seismic Engineering, it is estimated that about 80% of buildings in the city of Bogotá were built without complying with any seismic regulations (Centro de Estudios e Investigaciones Sobre Riesgo, 2005). If this happens in the capital of the country, it can be concluded that it also happens in the rest of the country.

Nowadays some of the most used solutions for structural retrofitting encompasses FRP (fibre reinforced polymer) and FRCM (fabric reinforced cementitious matrix). However, those techniques are expensive to develop in Colombia due to import and patent issues, making it difficult to expand their applications around the country. In addition, because of the differences in thermal and mechanical properties with concrete, especially under circumstances of moisture and terminal changes, these solutions can be detached from concrete, which invalidates them from external structural elements (Byars et al., 2001; Vega Vargas, 2015). Another usual solution for this problem consists in performing the seismic strengthening system of concrete structures by means of a steel jacketing (Ruiz-Pinilla et al., 2014). However, this option also must face the significant cost of the necessary steel.

On the one hand, a set of special traits, such as durability, ductility, and ease of application, render UHPFRC particularly attractive for the improvement and seismic retrofitting of concrete structures (Martin-Sanz et al., 2016). Several researches have demonstrated that, with a slight surface treatment of the old concrete, UHPFRC is able to develop a high bond strength as repair material (Dagenais et al., 2018; Martin-Sanz et al., 2016; Tayeh et al., 2013). Among others, this is due to the pozzolanic reaction of the amorphous silica oxide of the supplementary cementitious materials of its components (such as silica fume or recycled glass powder) and the portlandite crystals of the old concrete, thus creating a mechanical and chemical bond between both concretes (AlHallaq et al., 2017).

On the other hand, to lower costs and become viable, the development of UHPFRC dosages should be carried out based on locally available raw materials (Abellán et al., 2020b; Abellán-García, 2020c; Abellán-García, Núñez-López, Torres-Castellanos, et al., 2020). However, the key properties of UHPFRC containing hybrid blending fibres as well as several locally available supplementary cementitious materials require to be studied experimentally because of the unclear combination effects of these components (Zhang et al., 2017). Besides, it is important to highlight that laboratory tests are usually labor-intensive, time-consuming, and costly (Abellán-García, 2020c; Abellán-García, Fernández-Gómez, & Torres-Castellanos, 2020; Zhang et al., 2017). To reduce the experimental campaign and its associated costs and times, probabilistic models can be employed to predict the mechanical properties of concrete. However, these models cannot be applied when the approaching problem involves too many factors and the interrelations amidst them are too complex, unknown, or both (Chandwani et al., 2015; Ghafari et al., 2015; Zhang et al., 2017). In cases such as UHPFRC, using several types of fibres and supplementary cementitious materials, due to their large amount of components, the use of traditional techniques is unsuccessful in achieving the expected precision (Abellán-García, 2020c; Chandwani et al., 2015).

In the last decades, Artificial Neural Network (ANN) applications have spread due to their great ability to reproduce non-linear and unknown relationships between input and output data pairs (Abellán-García, 2020c; Abellán-García, Fernández-Gómez, & Torres-Castellanos, 2020). That is why those mathematical procedures have demonstrated their ability to be helpful in complex engineering issues (Abellán-García, 2020c; Abellán-García, Fernández-Gómez, & Torres-Castellanos, 2020; Khashman & Akpinar, 2017).

The first objective of this paper is to develop two models through the R language (R Core Team, 2018) to forecast the behaviour of UHPFRC under direct tensile strength, when concrete incorporates supplementary cementitious materials and different types of fibres (even hybrid blends of two different fibres). A single model will be created for each response, i.e. the energy absorption capacity ($g$) and maximum post-cracking strain ($\varepsilon_{pc}$). A total of 50 own experimental campaign data added to 550 published

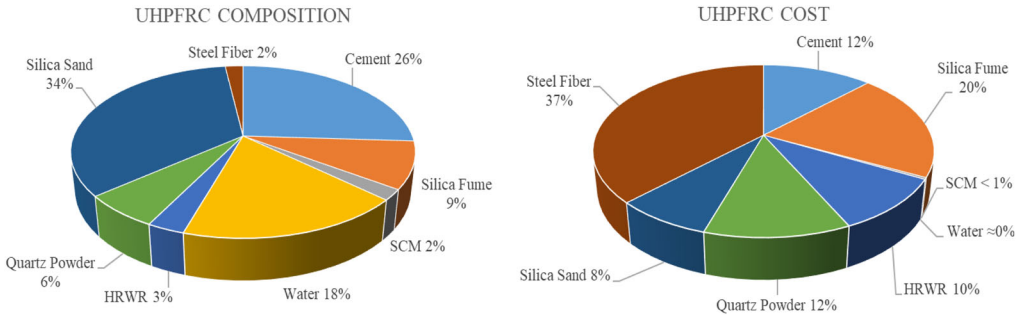


**Figure 1.** Average dosage of 150 dosages from the scientific literature.

works throughout the world data, totalising 600 data, were used for training purposes. To avoid overfitting, the models were adjusted by using the *k-fold* validation procedure. Once the two models were constructed and validated, a multi-objective algorithm was adopted to determine the optimum blend of locally available fibres in Colombia that, incorporated on a previously optimised high strength cementitious paste, result in the proper ductility properties for seismic retrofitting applications (i.e. $g \geq 50\,\text{kJ/m}^3$ and $\varepsilon_{pc} \geq 0.3\%$) at lower cost.

## 2. UHPFRC

Ultra-high-performance fibre reinforced concrete is a novel high-tech material developed over the last two decades (Abellan et al., 2018a; Abellán et al., 2020b; Abellán-García, Núñez-López, Torres-Castellanos, & Fernández-Gómez, 2019; Martin-Sanz et al., 2016; Soliman & Tagnit-Hamou, 2017a). It is a kind of high-tech fibre cementitious composite material with superb mechanical and durability properties compared to other types of concrete. Its excellent properties can be attributed to its high particle packing density, its low water to binder ratio, its selected materials and precise mixing processes, which leads to an extremely low porosity cementitious matrix (Abellan et al., 2018a; Abellán et al., 2020a). These extremely low porosity and low permeability characteristics of UHPFRC are mainly responsible of enhanced durability and mechanical properties over other types of concrete (Abbas et al., 2016; Abellan et al., 2018; Ghafari et al., 2014; Schmidt & Schmidt, 2012; Soliman & Tagnit-Hamou, 2017c). Laboratory tests indicate a superb compressive strength, which ranges from 150 to 200 MPa, while tensile strength without fibres lies in the range of 6–9 MPa (Abellan et al., 2018a, 2018b; Martin-Sanz et al., 2016). The overcoming of the brittleness of ultra-high performance concrete (UHPC) via addition of fibres also improves the material's toughness, and tensile and flexural capacity (Kou & Xing, 2012; Soliman & Tagnit-Hamou, 2017b). The effect of the fibres on UHPFRC's properties has a strong dependency on the content (1–6%), orientation, material, shape, length, and equivalent diameter of the fibre (Kou & Xing, 2012; Soliman & Tagnit-Hamou, 2017b).

Among others, the superb properties achieved by UHPFRC render it particularly attractive for both construction of new infrastructure such as footbridges, precast deck panel bridge joints, tunnel boring machine key-stones, special prestressed and precast concrete elements, marine platforms, precast walls, urban furniture, and other architectural applications, in addition to the improvement (rehabilitation, strengthening) of concrete structures, as well as overlay over damaged pavements and industrial floors (Abellán et al., 2020; Abellán-García, Nuñez-Lopez, & Arango-Campo, 2020; Acker & Behloul, 2004; Haber et al., 2017; Kalny et al., 2016; Martin-Sanz et al., 2016; Shaaban et al., 2016; Soliman & Tagnit-Hamou, 2017b).

### 2.1. Composition of UHPFRC

The use of exclusively raw materials in its composition is one of the main disadvantages of UHPFRC because of the increase of both carbon footprint and final cost of the material (Abellán et al., 2020a, 2020b; Ghafari, Costa, Nuno, et al., 2015; Tagnit-Hamou et al., 2016). This factor prevents a wider use of the material and especially its introduction in new markets.

A typical UHPFRC dosage is composed by Portland cement (C), silica fume (SF), quartz powder (QP), silica sand (SS) with a maximum size of 600 $\mu$m, high-range water reducers (HRWR) also known as superplasticizers, and steel fibre (De Larrard & Sedran, 2002; Richard & Cheyrezy, 1995; Tagnit-Hamou et al., 2016). Abellan et al.(2018b) showed an average UHPFRC dosage obtained from 150 UHPFRC mixtures from scientific articles, sharing the following characteristics in common: compressive strength over 150 MPa with no special curing conditions, maximum aggregate size between 0.5 and 0.6 mm, and 2% of steel fibre content in volume. This average dosage and the cost implication of its components calculated based on market prices in Colombia is depicted in Figure 1.

On the one hand, the high quantity of cement in UHPC (over 800 kg/m$^3$) has a detrimental impact on sustainability (Abdulkareem et al., 2018; Abellan et al., 2018a; Abellán-García et al., 2021; Richard & Cheyrezy, 1995). In fact, Portland cement, the principal hydraulic binder used worldwide in modern concrete, in addition to be a product of an energy-intensive industry (4 GJ/ton of cement) is also responsible for large emissions of $CO_2$, thus contributing to global warming (Abellán, Núñez-López, Torres-Castellanos, et al., 2020; Abellán-García et al., 2019, 2020b). Manufacturing one ton of Portland-cement clinker releases approximately one ton of $CO_2$ into the atmosphere, while nowadays the world's yearly cement output of 1.5 billion tons of mostly Portland cement is responsible of nearly 7% of global $CO_2$ emissions (Van Tuan et al., 2011). Therefore, one of the key sustainability challenges is to design and produce UHPFRC with less cement and in consequence lower $CO_2$ emissions than a traditional one, while providing the similar mechanical properties, and durability. On the other hand, it is important to note that only 2% by volume of steel fibre represents almost 40% of the total cost of the mixture.

### 2.2. Use of supplementary cementitious materials in UHPFRC

To address the cost and carbon footprint issues, at least partially, in the last decades, a great effort has been made in analysing the effect of supplementary cementitious materials in partial substitution of cement – because of $CO_2$ emissions – and silica fume – regarding the final cost of the mixture (Abellán et al., 2020a, 2020c; Abellán-García, Fernández-Gómez, & Torres-Castellanos, 2020; Abellán-García et al., 2020b). Among those, the work of Abellan et al. (2020a), who optimised a UHPC dosage by using locally available raw materials in Colombia, could be highlighted. In their work they showed a combined methodology that blends techniques such as neural networks data mining, design of experiments, and multi-objective optimisation to analyse the possibility of achieving compressive strength over 150 MPa without special curing conditions and limiting the content of silica fume to 100 kg/m$^3$. The supplementary cementitious materials used in this study included fly ash, ground granulated blast slag furnace, electric arc slag furnace, recycled glass powder, FC3R, metakaolin, and limestone powder. According to their results, the combination of limestone powder and recycled glass powder yield to a reduction of cement content of over 30% of the cement content and over 40% of the final cost when compared with a reference UHPC dosage with no more binder's component than cement and silica fume. This optimised cementitious matrix will be the one used in the multi-objective optimisation section of this research.

On the other hand, the use of supplementary cementitious materials as partial substitution of silica fume also presented an improvement in some durability properties, such as autogenous shrinkage and permeability (Ghafari et al., 2012).

From the above, it can be concluded that it is possible to reduce the carbon footprint and the cost of the UHPFRC cementitious matrix (Abellán et al., 2020a; Ghafari et al., 2012). However, it will be necessary to evaluate the locally available raw materials in each case.

### 2.3. Ductility of UHPFRC

Ductility is the most important feature of UHPFRC for seismic retrofitting applications (Chao, 2016; Dogan & Krstulovic-Opara, 2003; Khan et al., 2018; Kim et al., 2009; Massicotte et al., 2013). Ductility of UHPFRC is usually measured by direct tensile tests (Soranakom & Mobasher, 2008; Kwon et al., 2014; Massicotte et al., 2013; Wille et al., 2014). Regarding direct tensile tests behaviour, UHPFRC can be classified as strain-softening or strain-hardening (Pyo et al., 2016; Wille et al., 2011). The fibres' bridging effect significantly affects performance in the hardening and softening domain [13). In accordance with Naaman (Naaman & Reinhardt, 2007), strain hardening happens as output of the maximum post-cracking tensile

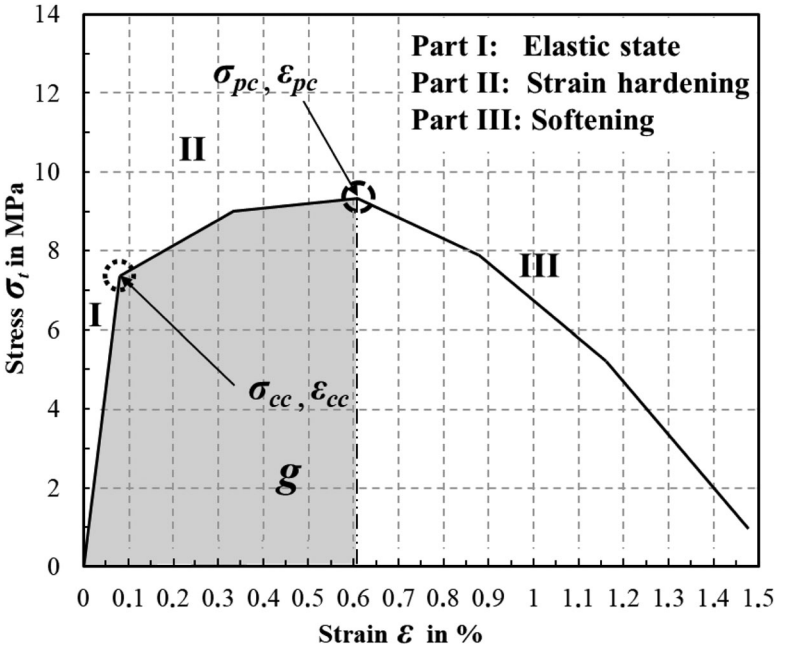


**Figure 2.** Idealised strain hardening UHPFRC behavior under direct tensile test.

strength, $\sigma_{pc}$, exceeding the cracking tensile strength, $\sigma_{cc}$. Equation (1) depicted strain hardening condition, that is:

$$\sigma_{pc} \geq \sigma_{cc} \tag{1}$$

Figure 2 shows how the tensile behaviour of UHPFRC could be explained by three different phases, as follows (Wille et al., 2011, 2014). Zone I, elastic behaviour up to cracking strength $\sigma_{cc}$ which produces first crack, followed by activation of fibres as result of the development of several micro cracks (multi-cracking phenomenon). The stress level is characterised by $\sigma_{cc}$, its associated strain $\varepsilon_{cc}$ and $E_{cc}$ where the material enters its strain hardening behaviour. Zone II, or the domain of strain-based hardening with multiple cracking, whose evolution is ruled by the fibres, affected by the dissipated energy per unit volume $g$, which is the area under the stress–strain curve up to $\sigma_{pc}$ and its associated strain $\varepsilon_{pc}$. Finally, Zone III or the softening behaviour domain which can be characterised by the slip of the fibre until the pullout.

On the one hand, according to Wille et al. (Wille et al., 2014), a value of $g \geq 50\,kJ/m^3$ is suggested to define performance of high energy absorbing UHPFRC. On the other hand, it should be noted that in structural applications which involves both UHPFRC and conventional steel bar reinforced concrete, such as seismic retrofitting of non-ductile existing structures, accomplishing $\varepsilon_{pc} \geq 0.3\%$ would assure that the UHPFRC fully contributes until and further than the yielding of bars (Wille et al., 2011). Therefore, the ductility properties to be met in the multi-objective optimisation algorithm for seismic retrofitting applications of UHPFRC will be $g \geq 50\,kJ/m^3$ and $\varepsilon_{pc} \geq 0.3\%$, thus, ensuring high ductility and the contribution of the UHPFRC beyond the steel yield of the concrete structure reinforcement to be retrofitted.

### *2.4. Fibres in UHPFRC*

As the UHPC matrix is very brittle, fibre reinforcement is added to obtain tensile ductility and strain hardening behaviour (61). Typical UHPFRC has fibre contents of 2 % or above by volume. The maximum fibre content to achieve the proper ductility parameters is a function of the fibre aspect ratio ($l_f/d_f$ , where $d_f$ and $l_f$ represent the equivalent diameter and the length of the fibre respectively), material and shape, and even if there is a mixture of different fibres looking for synergies between them (ACI Committe 239R, 2018; Kwon et al., 2014; Wille et al., 2011).

Table 1. High strength twisted steel fibres used in special UHPFRC dosages in scientist literature.

| Reported high strength steel twisted fibres | | | | | |
|---|---|---|---|---|---|
| Number of twists per total length | $d_f$ (mm) | $l_f$ (mm) | $l_f/d_f$ | Tensile strength (MPa) | Reference |
| 16 | 0.30 | 30 | 100 | ≈2100 | Wille et al. (2011) |
| 6-8 | 0.30 | 30 | 100 | ≈3100 | Wille et al. (2011) |
| n/a | 0.30 | 25 | 83 | ≈2670 | Pyo et al. (2016) |
| n/a | 0.30 | 18 | 60 | ≈2600 | Wille et al. (2014) |
| n/a | 0.20 | 20 | 100 | ≈3000 | Ryu et al. (2012) |
| | 0.22 | 22 | 100 | ≈3000 | Ryu et al. (2012) |
| n/a | 0.30 | 30 | 100 | ≈3000 | Ryu et al. (2012) |
| n/a | 0.30 | 30 | 100 | ≈2500 | Yoo and Kim (2019) |

However, in budget terms, although the partial replacement of cement and silica fume can help lower the final cost of the mixture, it is important to note that the greatest weight in this cost is represented by the content of steel fibre (see Figure 1). Thus, reducing the amount of fibres needed, the total cost of the fibres, or both is a challenge for engineers.

Some of the ways to face that problem consists in the use of high-technology fibres, particularly high strength twisted steel fibres (Kim et al., 2009; Pyo et al., 2016; Wille et al., 2011, 2014). The characteristics of those special fibres reported in scientific literature can be observed in Table 1.

The use of such special fibres allows to achieve outstanding properties of UHPFRC even with only 1% of volume content (Ryu et al., 2012; Wille et al., 2011), which represents an important reduction in fibre content in comparison to the dosage depicted in Figure 1. However, these steel fibres reported here were homemade high strength twisted steel fibres (Kim et al., 2009; Pyo et al., 2016; Wille et al., 2011; 2014), not even commercially available in the most developed countries.

Another way to address the fibre issue is through the hybrid blending of fibres. The effect of blending fibres on the behaviour of UHPFRC was the focus of several studies (Ghafari et al., 2014; Kim et al., 2011; Kwon et al., 2014; Park et al., 2012; Yu et al., 2015). Their results showed the synergy achieved by the mixture of micro and macro fibres which lead to a higher efficiency of the overall use of fibres in this type of concrete.

Finally, a less explored option would be the use of low-cost fibres. In this case, the use of fibres is greater, but the final cost of the total fibres remains below the cost of higher quality fibres with a lower volume. This option is very interesting in cases of developing countries where import costs are usually high (Abellán-García et al., 2021).

The present study addresses the question through an analysis of the last two options considering mixing up to two different types of fibre in a previously optimised UHPC matrix.

## 3. Neural networks

The simplest architecture of a neural network model was the perceptron, devised by Rosenblant (1958). Perceptron is composed of one neuron which processes information from two inputs and produces one output (Ghafari, 2012). It is defined as a four-tuple entity (i.e. sensors that (i) receive inputs, (ii) multiply them by weights, (iii) a function collecting all the weighted data to produce a measurement on the impact of the observed phenomenon, and (iv) a constant threshold). Ascertaining these weights to produce a particular result is known as 'training the model', which is the methodology that allows the model to learn (Estebon, 1997). Figure 3 shows the schematic diagram of perceptron structure.

For more complex applications, multi-layer perceptron (MLP) is employed, which could contain one or more hidden layers in addition to the input and output layers. The multilayer perceptron has been a commonly used neural network architecture (Abellán-García, 2020a; Aderaw et al., 2018; Chandwani et al., 2015; Gupta, 2013).

In the engineering field, MLP models have been employed in applications like detection of structural damage, water resources engineering, traffic engineering, structural system identification, material behaviour modelling, concrete mix proportioning, and concrete strength forecasting (Adeli, 2001; Aderaw et al., 2018). In fact, the application of artificial neural networks to forecast mechanical properties of pastes, mortars, and concretes had become one of the most fertile fields in the scientific literature of civil engineering production (Chandwani et al., 2014). However, until now, few investigations have been conducted

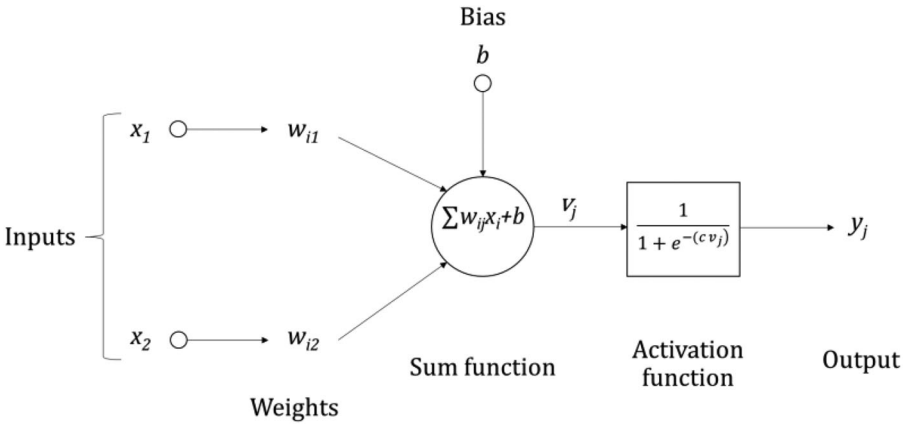


**Figure 3.** Schematic diagram of perceptron structure.

on forecasting the performance of UHPC/UHPFRC using neural networks. Among those Abellán-García (2020c), Zhang et al. (2017), Abellán-García, Fernández-Gómez, and Torres-Castellanos (2020), Ghafari et al. (2015), Taghaddos et al. (2004), and Abellán-García et al. (2020) investigations can be highlighted, as presented in Table 2.

As far as the authors are aware, there is no previous work dealing with the neural network-based prediction tool to forecast the direct tensile behaviour of UHPFRC.

## 4. Databases

### 4.1. Data collection

Datasets containing dosages and direct tensile behaviour of UHPFRC were collected from several international symposiums on high and ultra-high-performance concrete (including Kassel 2004, 2008, 2012 and 2016), PhD dissertations, and other published works. Only those dosages with information of the dissipated energy per unit volume $g$ or the necessary data to its calculation (i.e. $\sigma_{cc}$ , $\varepsilon_{cc}$ , $\sigma_{pc}$ , and $\varepsilon_{pc}$) were collected, totalising 550 observations from scientific literature. In addition, 50 experimental tests with different combinations of locally available fibres in Colombia were performed in various laboratories. The cementitious matrix used in the test corresponds to a previously optimised ultra-high performance cementitious matrix (Abellán et al., 2020a). As a result, the present investigation has had a total of 600 observations for the development of the artificial neural network models.

The database includes both dosages with a single type of fibre (referred to in the database as fibre 1), and UHPFRC's dosages with hybrid binary fibre mixtures (fibre 1 and fibre 2).

The presence of qualitative variables in the database, specifically the type of fibre, has been resolved using *dummy* or dichotomous variables, the value of which is 1 if the fibre is of the type considered and 0 otherwise.

The independent variables (which will be the input variables for the neural network models) collected in the database, as well as their coding can be seen in Table 3.

With the proposal to subtract possible mathematical effects of the fibre ordering in the UHPFRC mix, the considered database has been duplicated by swapping the fibre ordering.

### 4.2. Outliers treatment

Before adjusting the artificial neural network, it is necessary to deal with outliers, as they can greatly affect the resulting model (Atkinson & Riani, 2000). Therefore, a descriptive statistical analysis was performed on each variable to point out outliers (Härdle & Simar, 2012). Unusual distributions (skewness), data entry errors, and outliers in the data were identified employing bagplots. Bagplots (or bivariate boxplots) are two-dimensional equivalent of single variable boxplots that are utilised to spot anomalous data and outliers by robust methods, drawing ellipses that lay out possible inconsistent observations (Abellán-

**Table 2.** Scientific literature references on applications of ANN to predict mechanical properties of UHPC/UHPFRC.

| ANN Architecture | Number of observations in dataset | Output(s) | Reference |
|---|---|---|---|
| 4-2-2-1 | 38 | 12-day compressive strength under heat treatment | Taghaddos et al. (2004) |
| 7-15-3 | 53 | Slump Flow, 28-day compressive strength, 2-day compressive strength under heat treatment | Ghafari et al. (2015) |
| 11-10-4 | 78 | 7, 28, 90- and 365-day compressive strength | Zhang et al. (2017) |
| 11-4-4-4-1[a] | 696 | Limit of Proportionality (LOP), its corresponding deflection ($\delta_{LOP}$), Modulus of Rupture (MOR), and its corresponding deflection ($\delta_{MOR}$) of UHPFRC under bending test | Abellán-García et al. (2020) |
| 17-4-2-1 | 927 | 28-day compressive strength | Abellán-García (2020) |
| 17-4-1 | 604 | 1-day compressive strength | Abellán-García (2021) |
| 12-10-5-1[b] | 265 | Slump Flow, 1, 7, and 28-day compressive strength | Abellán-García et al. (2020) |
| 12-9-5-1[c] | | | |
| 12-4-2-1[d] | | | |
| 12-4-4-1[e] | | | |

[a]Four different models with the same architecture, one model for each response.
[b]Model for slump flow.
[c]Model for 1-day compressive strength.
[d]Model for 7-day compressive strength.
[e]Model for 28-day compressive strength.

García & Guzmán-Guzmán, 2021; Everitt & Hothorn, 2015). Nonetheless, having confidence in the use of this procedure without a critical analysis of the data could also be a dangerous practice. Some of the suspicious points indicated by bagplots could be depicting the real behaviour of the data, while the rest of the observations could just be clumped together very closely. Figure 4 depicts the bagplot for the pair of variables energy absorption capacity $g$ (expressed in kJ/m$^3$) and total fibre factor $\chi_T$. The graph shows as possible anomalies some dosages with PVA monofilament microfibers (see Figure 8h) whose diameter is less than 50 microns, when located outside the ellipse. However, its location outside the ellipse is only due to the low value of its diameter, which leads to a high value of $\chi_T$ and not because it really was inconsistent data. For this reason, removing this data would result in a loss of important information.

Once this procedure was completed, 95 observations were eliminated from the database, leaving 505 for training and validation purposes.

### 4.3. Data normalisation

After the outliers were removed from the database, the next step consists in data normalisation. The input data and output data usually comprise of different identities either having no or minimum similarities. Normalisation of data removes the possibility of neural network bias towards the different identities and scales down all the input and output data. In this study, linear scaling in the range [0, 1] has been used as depicted in Equation (2).

$$x_{norm-sigmoid} = \frac{x - x_{min}}{x_{max} - x_{min}} \tag{2}$$

where $x_{norm}$ represents the normalised value of the variable $x$, $x_{max}$, and $x_{min}$ represent the minimum and maximum values of variable $x$, respectively.

Table 4 shows the range of variation and other statistics of all independent variables considered in this research.

**Table 3.** Input variables: Coded and description.

| Coded variable | Description | Coded variable | Description |
|---|---|---|---|
| X1 | Cement content in kg/m$^3$ | X18 | Tensile strength of fibre 1 in MPa |
| X2 | Silica fume content in kg/m$^3$ | X19 | Length of fibre 1 in mm ($l_{f1}$) |
| X3 | Supplementary cementitious materials (without considering either cement or silica fume) in kg/m$^3$ | X20 | Equivalent diameter of fibre 1 in mm ($d_{f1}$) |
| X4 | Quartz powder content in kg/m$^3$ | X21 | fibre volume fraction of fibre 1 in % ($V_{f1}$) |
| X5 | Water content in kg/m$^3$ | X22 | fibre factor of fibre 1 expressed as $\chi_{f1} = V_{f1} \times l_{f1}/d_{f1}$ |
| X6 | Superplasticizer content in kg/m$^3$ | X23 | Dummy variable whose value is 1 if fibre 2 is a straight steel fibre and 0 otherwise |
| X7 | Sand content in kg/m$^3$ | X24 | Dummy variable whose value is 1 if fibre 2 is a hooked end steel fibre and 0 otherwise |
| X8 | Maximum size of sand in μm | X25 | Dummy variable whose value is 1 if fibre 2 is a twisted steel fibre and 0 otherwise |
| X9 | Water to binder ration (w/b) | X26 | Dummy variable whose value is 1 if fibre 2 is a polyethylene fibre and 0 otherwise |
| X10 | Total fibre volume fraction in % | X27 | Dummy variable whose value is 1 if fibre 2 is a polypropylene fibre and 0 otherwise |
| X11 | Total fibre factor defined as $\chi_T = \chi_{f1} + \chi_{f2}$ | X28 | Dummy variable whose value is 1 if fibre 2 is a PVA fibre and 0 otherwise |
| X12 | Dummy variable whose value is 1 if fibre 1 is a straight steel fibre and 0 otherwise | X29 | Tensile strength of fibre 2 in MPa |
| X13 | Dummy variable whose value is 1 if fibre 1 is a hooked end steel fibre and 0 otherwise | X30 | Length of fibre 2 in mm ($l_{f2}$) |
| X14 | Dummy variable whose value is 1 if fibre 1 is a twisted steel fibre and 0 otherwise | X31 | Equivalent diameter of fibre 2 in mm ($d_{f2}$) |
| X15 | Dummy variable whose value is 1 if fibre 1 is a polyethylene fibre and 0 otherwise | X32 | fibre volume fraction of fibre 2 in % ($V_{f2}$) |
| X16 | Dummy variable whose value is 1 if fibre 1 is a polypropylene fibre and 0 otherwise | X33 | fibre factor of fibre 2 expressed as $\chi_{f2} = V_{f2} \times l_{f2}/d_{f2}$ |
| X17 | Dummy variable whose value is 1 if fibre 1 is a PVA fibre and 0 otherwise | X34 | Compressive strength of concrete in MPa |

## 5. Experimental research

### *5.1. Ultra-high-performance cementitious matrix (UHPC)*

For the experimental campaign a previously optimised eco-friendly ultra-high-performance concrete (UHPC) with low cement content was used (Abellán et al., 2020a; Abellán-García, 2020b). The proposed mixture used recycled glass powder and micro-limestone powder as partial substitution of cement and silica fume, optimising the mixture's packing density, leading to a compressive strength of 156 MPa under

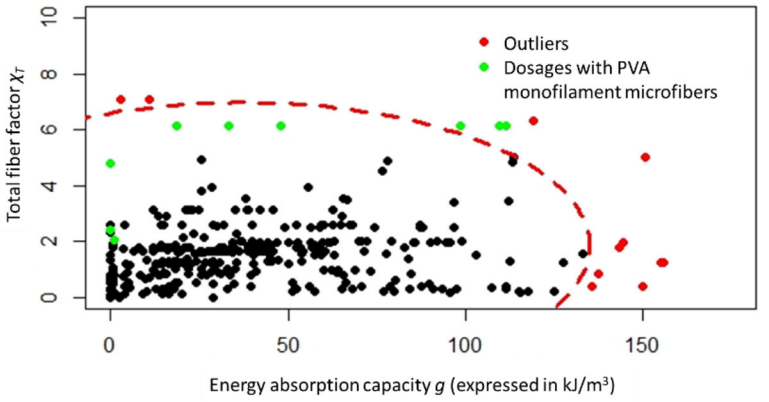


**Figure 4.** Bagplot for the pair of variables g and $\chi_T$.

**Table 4.** Statistics of the input variables considered in this research.

| Coded variable | $X_{max}$ | $X_{min}$ | Mean | Standard deviation | Coded variable | $X_{max}$ | $X_{min}$ | Mean | Standard deviation |
|---|---|---|---|---|---|---|---|---|---|
| X1 | 1,412.90 | 511.62 | 765.72 | 247.63 | X18 | 3,250.00 | 0.00 | 1,490.23 | 1,203.92 |
| X2 | 701.27 | 42.00 | 164.22 | 64.00 | X19 | 62.00 | 0.00 | 12.49 | 12.21 |
| X3 | 898.75 | 0.00 | 225.08 | 282.91 | X20 | 0.80 | 0.00 | 0.14 | 0.18 |
| X4 | 430.00 | 0.00 | 84.09 | 110.91 | X21 | 5.00% | 0.00% | 0.93% | 0.89% |
| X5 | 392.39 | 119.40 | 222.12 | 68.37 | X22 | 6.15 | 0.00 | 0.82 | 1.23 |
| X6 | 40.03 | 9.97 | 25.76 | 10.56 | X23 | 1.00 | 0.00 | 0.22 | 0.42 |
| X7 | 1,512.95 | 0.00 | 751.11 | 263.82 | X24 | 1.00 | 0.00 | 0.10 | 0.27 |
| X8 | 3,750.00 | 0.00 | 481.07 | 536.63 | X25 | 1.00 | 0.00 | 0.11 | 0.30 |
| X9 | 0.31 | 0.11 | 0.22 | 0.10 | X26 | 1.00 | 0.00 | 0.11 | 0.30 |
| X10 | 5.00% | 0.00% | 1.86% | 0.65% | X27 | 1.00 | 0.00 | 0.02 | 0.12 |
| X11 | 6.34 | 0.00 | 1.77 | 1.42 | X28 | 1.00 | 0.00 | 0.09 | 0.28 |
| X12 | 1.00 | 0.00 | 0.22 | 0.42 | X29 | 3,250.00 | 0.00 | 1,490.23 | 1,203.92 |
| X13 | 1.00 | 0.00 | 0.10 | 0.27 | X30 | 62.00 | 0.00 | 12.49 | 12.21 |
| X14 | 1.00 | 0.00 | 0.11 | 0.30 | X31 | 0.80 | 0.00 | 0.14 | 0.18 |
| X15 | 1.00 | 0.00 | 0.11 | 0.30 | X32 | 5.00% | 0.00% | 0.93% | 0.89% |
| X16 | 1.00 | 0.00 | 0.02 | 0.12 | X33 | 6.15 | 0.00 | 0.82 | 1.23 |
| X17 | 1.00 | 0.00 | 0.09 | 0.28 | X34 | 230.00 | 98.12 | 151.68 | 24.92 |

normal curing conditions (Abellán et al., 2020a). The introduction of micro-limestone powder and recycled glass powder not only allowed the partial replacement of cement and silica fume, but also led to a lower need for superplasticizer (Abellán et al., 2020b), consequently providing a more sustainable UHPC, at lower cost and with satisfactory mechanical properties (Abellán et al., 2020a). The dosage proportions for plain UHPC are given in Table 5. Some relevant information is depicted below:

- Cement was Type III ASTM with a $C_3S$ content of 65%, an average particle size ($d_{50}$) of 8 μm, a specific gravity of 3.15, and a low $C_3A$ content (<5%).
- Silica fume employed in this research is characterised by an exceedingly high $SiO_2$ content (92.3%), a specific gravity of 2.20, and an average particle size of 0.15 μm.
- Micro-limestone powder with an average particle size of 2.1 μm and a specific gravity of 2.73 was utilised as partial substitution of expensive silica fume.
- The average particle size of the recycled glass powder used was 28 μm and its specific gravity 2.55. Glass powder was obtained by grounding locally available recycled glass with a jet mill.
- The proportion of cement:silica fume:micro-limestone powder:glass powder was 1:0.17:0.39:0.55.
- A superplasticizer based on polycarboxylate ether was selected because it produced the best settling flow and enhanced air release from the pulp at the lowest content.
- The optimum water to binder ratio was determined to be 0.16.
- Silica sand with a specific gravity of 2.65, maximum particle size ($d_{max}$) of 600 μm, and d50 of 165 μm, was used. The proportion of cement:silica sand was 1:1.50

**Table 5.** Mixture for UHPC used in this study (Abellán et al., 2020).

| Properties and proportions by weight of cement of UHPC | | | | | | | | |
|---|---|---|---|---|---|---|---|---|
| Cement | Silica fume | Micro-limestone powder | Recycled glass powder | Water | Superplasticizer | Silica sand | VPD[a] | $f_c$ (MPa) |
| 1.00 | 0.17 | 0.39 | 0.55 | 0.31 | 0.0054 | 1.50 | 0.81 | 156 |

[a]Virtual Packing Density (VPD) according to Larrard (De Larrard & Sedran, 2002; De Larrard,1999; Larrard, 1994).

**Table 6.** Chemical characterisation and properties of cement, silica fume, micro limestone powder, recycled glass powder and silica sand.

| Properties of UHPC's components | | | | | |
|---|---|---|---|---|---|
| Chemical analysis | Cement | Silica fume | Micro-limestone powder | Recycled glass powder | Silica sand |
| Specific gravity (g/cm$^3$) | 3.16 | 2.20 | 2.73 | 2.55 | 2.65 |
| Loss of ignition (%) | 2.58 | 0.60 | 42.21 | 1.00 | 0.20 |
| $SiO_2$ (%) | 19.42 | 92.29 | 0.90 | 72.89 | 99.80 |
| $Al_2O_3$ (%) | 4.00 | 0.59 | 0.10 | 1.67 | 0.14 |
| CaO (%) | 64.42 | 3.89 | 55.51 | 9.73 | 0.17 |
| MgO (%) | 1.52 | 0.26 | 0.70 | 2.08 | 0.01 |
| $SO_3$ (%) | 1.93 | 0.07 | 0.10 | 0.01 | – |
| $Na_2O$ (%) | 0.19 | 0.31 | 0.03 | 12.54 | – |
| $K_2O$ (%) | 0.39 | 0.54 | 0.00 | 0.76 | 0.05 |
| $TiO_2$ (%) | 0.38 | 0.01 | 0.00 | 0.04 | – |
| $Mn_3O_4$ (%) | 0.05 | 0.01 | 0.01 | 0.01 | – |
| $Fe_2O_3$ (%) | 3.61 | 0.24 | 0.05 | 0.81 | 0.04 |

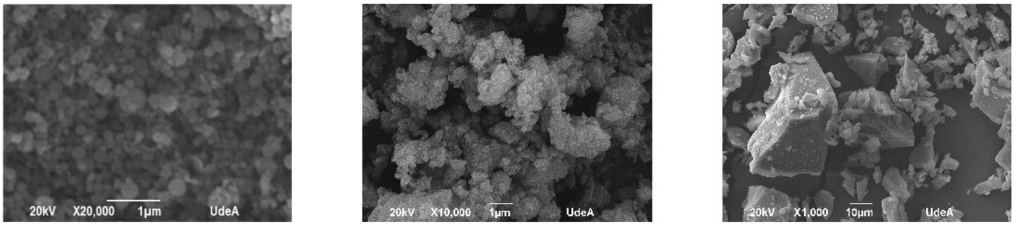


(a) (b) (c)

**Figure 5.** SEM of supplementary cementitious materials used in research: (a) silica fume; (b) micro-limestone powder; and (c) recycled glass powder.

Table 6 depicts the chemical composition of the materials used in this study. The analysis trough scanning electron microscopy (SEM) of the supplementary cementitious materials is displayed in Figure 5. Because of the average particle size of recycled glass powder is over ten times higher than the average particle size of micro-limestone powder, which is almost twenty times higher than the silica fume particle, it was necessary to employ different magnifications in the SEM images to appreciate the characteristics of the particles of these components. Results pointed out the lack of porosity of the recycled glass powder, the rough surface of the micro-limestone powder particle, and the spherical shape together with small size of the silica fume particles.

Figure 6 presents the X-ray powder diffraction (XRD) of the cement and the cementitious materials. Figure 6a shows the mineralogical analysis obtained for the cement. The XRD pattern for silica fume is depicted in Figure 6b. The intense broad peak observed for silica fume pointed out that this material is totally amorphous. The analysis exhibited in Figure 6c shows a majority composition of calcite for the limestone powder. The XRD analysis performed on the recycled glass powder (Figure 6d) revealed its amorphous nature.

The particle size distribution (PSD) of the components and the A&A$_{mod}$ curve (Funk & Dinger, 1994) obtained by using a q value of 2.64 (Abellan et al., 2018) is depicted in Figure 7. The A&A$_{mod}$ curve (Funk

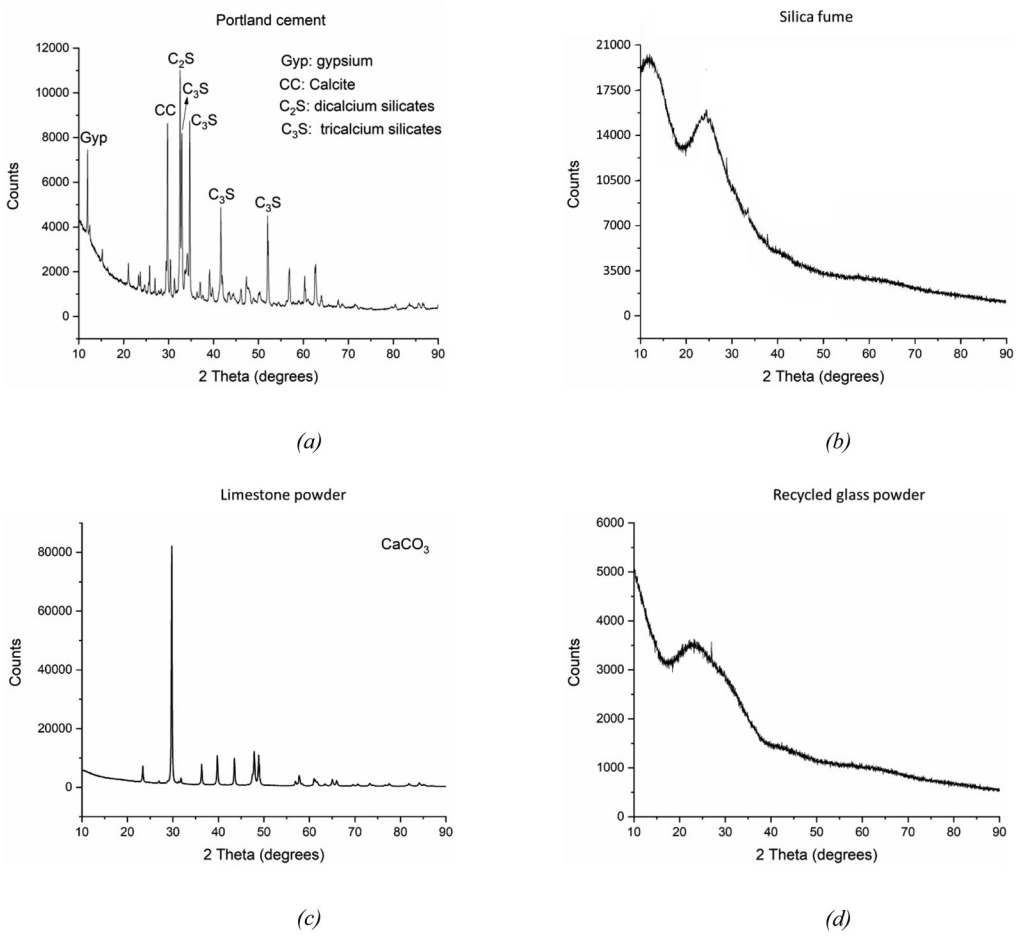


**Figure 6.** XRD of: (a) cement; (b) silica fume; (c) micro-limestone powder; and (d) recycled glass powder.

& Dinger, 1994) is one of the most used packing models for the design of UHPC and UHPFRC mixtures (Abellán et al., 2020b; Abellan-Garcia, Núñez-López, Torres-Castellanos, N., & Fernández-Gómez, 2020; Abellán-García et al., 2019).

### *5.2. Fibres*

Straight high strength ($\sigma_{fu} \geq 2100$ MPa) steel fibres were used in this study (see Table 7), with an aspect ratio of 65 ($l_f$/df = 13/0.2 mm) and 30 ($l_f$/df = 6/0.2 mm). Those fibres are the most used worldwide for UHPFRC dosages.

In addition, three types of commercially available non-high strength steel ($\sigma_{fu} \leq 2100$ MPa) deformed steel fibres and three types of polymeric fibres were included. On the one hand, the normal strength steel fibres encompass two types of hooked end and a twisted one. In hooked end fibres, its hook deformation at the end of the fibre provides a mechanical bond at the end, while an uniformly distributed deformation over the entire twisted fibre length, provides a mechanical bond along the entire fibre length (Kim et al., 2009; Pyo et al., 2016; Wille et al., 2014 ). Two types of commercially available hooked fibres were utilised ($l_f/d_f$ = 35/0.50 mm, and $l_f/d_f$ = 60/0.75), in which the mechanical bond is controlled by the resistance of the hooked end to straightening, when subjected to pull-out. A unique type of twisted fibre ($l_f/d_f$ = 13/0.50 mm) was found in the Colombian market.

On the other hand, the polymeric fibres considered involve two macro-fibres, one of polypropylene and the other of polyethylene, as well as a fibrillated polyvinyl alcohol (PVA) microfiber

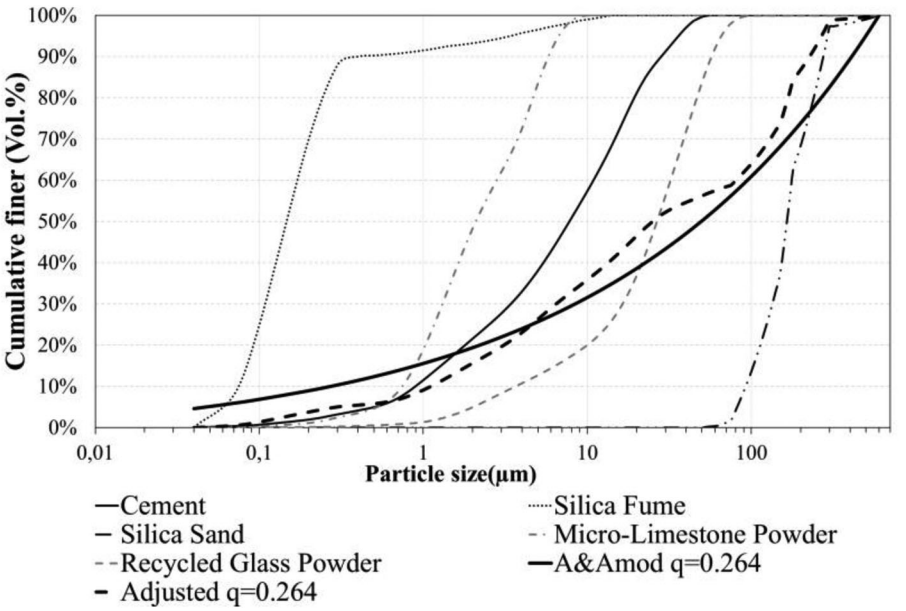


**Figure 7.** Particle size distribution of the matrix materials, target and mix curve.

**Table 7.** Properties of steel fibres used in this study.

| Notation | Form | $d_f$ (mm) | $l_f$ (mm) | $d_f/l_f$ | Material | Tensile strength (MPa) | Cost (COP/kg)[a] |
|---|---|---|---|---|---|---|---|
| $S_1$ | Straight | 0.20 | 13 | 65 | Steel | ≈2600 | 11,000 |
| $S_2$ | Straight | 0.20 | 6 | 30 | Steel | ≈2600 | 10,500 |
| $H_1$ | Hooked | 0.50 | 35 | 70 | Steel | ≈2000 | 9,000 |
| $H_2$ | Hooked | 0.75 | 60 | 80 | Steel | ≈1600 | 4,855 |
| T | Twisted | 0.50 | 13 | 26 | Steel | ≈1700 | 7,500 |
| PP | Straight | 0.72 | 48 | 75 | Polypropylene | ≈650 | 30,000 |
| PE | Straight | 0.67 | 50 | 67 | Polyethylene | ≈550 | 27,000 |
| PVA | Straight | 0.025 | 6 | 240 | Polyvinyl alcohol | ≈1600 | 35,000 |

aEstimated cost in the Colombian market and expressed in Colombian pesos per kilo.

The detailed information of used fibres is summarised in Table 7 and Figure 8.

It is important to note that although the prices per kilogram of polymeric fibres are higher than those of steel fibres, the dosage of concrete is done by volume, where the density of the material plays an important role.

### *5.3. Blending procedure, casting, and curing*

Cement, silica fume, micro-limestone powder, glass powder, water, high-range-water-reduce superplasticizer (HRWR) and steel fibres were mixed together in a 11-liter Hobart type mixer according to the following methodology: first, all cementitious materials were dry-mixed for about 10 minutes. Water that was previously pre-blended with HRWR was then incorporated gradually and mixed for another 5 minutes. After that, sand was also gradually added and mixed for another 3 minutes. Finally, fibres were incorporated and the whole concrete was blended for 2 more minutes. After blending, the cement mixture with fibres was then placed in a JSCE (Yokota et al., 2008) dog bone mould to full capacity applying slight vibration during the pouring and 1 minute after. It is important to note that the small dimensions of the JSCE dog bone specimen (see Figure 9) in height (30 mm) and width (30 mm) compared to the length of the fibres (from 6 to 60 mm) leads to a positioning of the fibres in a preferential way, with most fibres aligned along each specimen's major axis, which is the direction of the applied tensile load.

After casting the UHPFRC into the dog bone moulds, the specimens were covered with plastic lids and squirrelled away at room temperature for 24 h. After 24 hours, the specimens were taken out of their

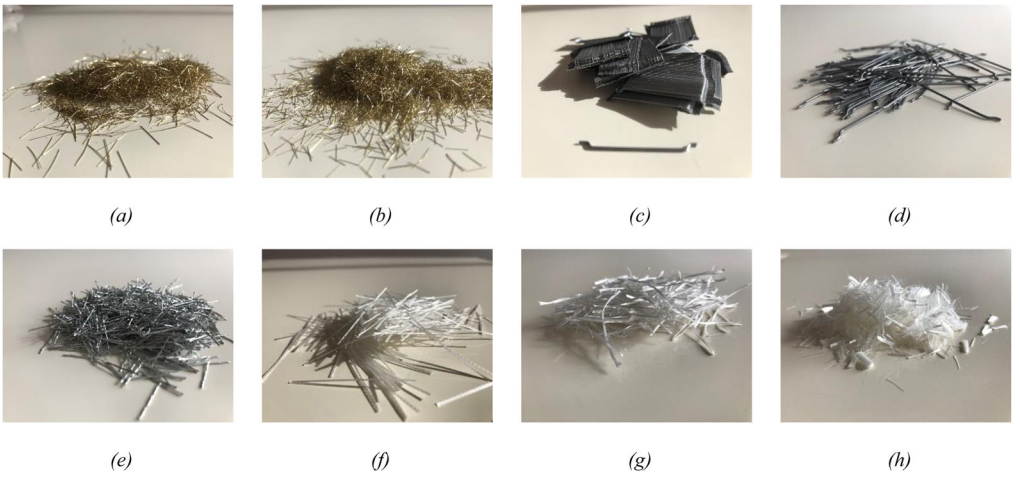


**Figure 8.** Different types of steel fibres used in this research: (a) high strength steel straight $l_f/d_f = 13/0.20$ mm ($S_1$); (b) high strength steel straight $l_f/d_f = 13/0.20$ mm ($S_2$); (c) normal strength steel hooked lf/df = 35/0.50 mm ($H_1$), (d) normal strength steel hooked $l_f/d_f = 60/0.75$ mm ($H_2$); (e) normal strength steel twisted $l_f/d_f = 13/0.50$ mm (T); (f) polypropylene $l_f/d_f = 48/0.72$ mm (PP); (g) polyethylene $l_f/d_f = 50/0.67$ mm (PE); and (h) polyvinyl alcohol $l_f/d_f = 6/0.025$ mm (PVA).

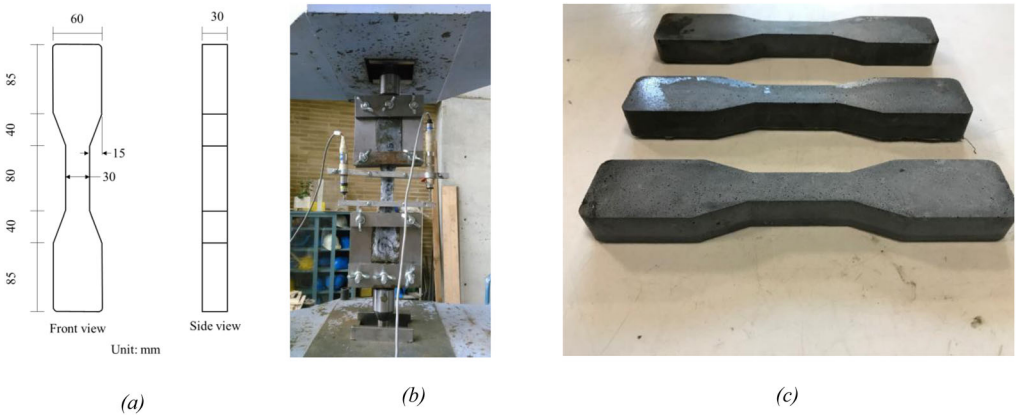


**Figure 9.** Direct tensile specimen and setup.

moulds and cured in a moisture room at 20°C until reaching a designed age of 28 days. The direct tensile tests were performed at the age of 28 days.

### *5.4. Test setup*

The geometry of the dog bone specimen, also the system presented in Figure 9, was established according to the JSCE-08 (Yokota et al., 2008). The section of the tensile specimens employed was 30 × 30 mm. Each specimen was evaluated with a gage length of 75 mm. No steel wire mesh was used as reinforcement at the ends of the specimens to avoid the failure of specimens out of gage length. The alignment of the tensile set-up was carefully verified before testing by using a plumb. The specimens were installed with care to avoid any influence of eccentricity. A universal testing machine performing displacement control was used to run the tensile tests. The tensile tests were conducted at a fixed speed of displacement of 0.5 mm/min according to JSCE-08 (Yokota et al., 2008). The boundary conditions at ends of the tensile test set-up were one end fixed and another end loaded. Two linear variable differential transformers (LVDT) were placed on both sides of the specimen, to measure its elongation. The average value

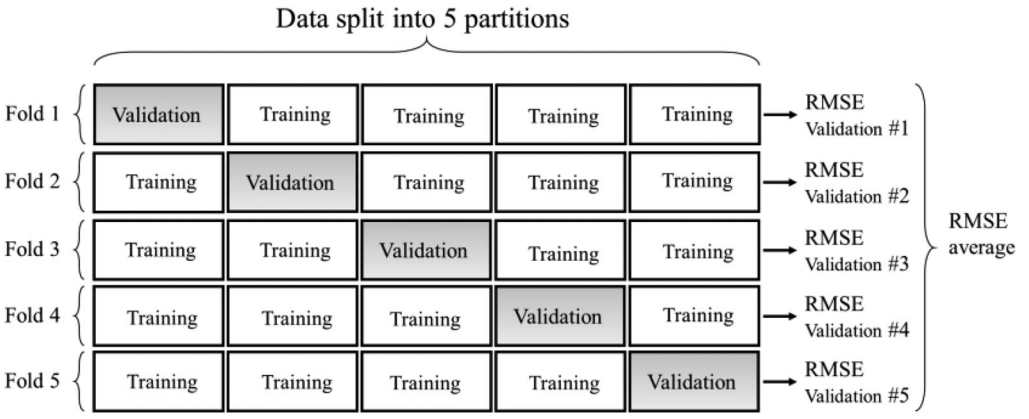


Figure 10. *k-fold* validation (Chollet & Allaire, 2018).

from the two LVDTs was utilised in the calculation of the tensile strain in the gauge region, up to the point it reached the peak tensile stress. The load signal was measured from a load cell that was directly fixed to the bottom of the cross head. Three samples were evaluated for each fibre combination, hence the reported values of $g$ (kJ/m$^3$) and $\varepsilon_{pc}$ (%).

## 6. Analytical research

### 6.1. Cross validation

To facilitate training and testing of the artificial neural network models, the obtained database was randomised and divided into training and test datasets. 379 observations were utilised for training purposes and the remaining 126 were utilised for testing the trained models. Both subsets contained all the possible types of fibres considered.

Besides, to evaluate the neural network model while keeping its parameters adjusted (such as the number of neurons in the hidden layers), the training data could be divided into a training and a validation set. Nonetheless, since there are such few data observations, the validation set would end up being small for a neural network validation (as in our case). Therefore, the validation scores might change a lot depending on which data points were chosen to use for validation and which were selected for training, that is, the validation scores might have a high variance regarding the validation division. This would prevent from reliably assessing the model (Abellán-García et al., 2021; Chollet & Allaire, 2018).

The best practice in such situations is to utilise *k-fold* cross-validation (see Figure 10). It is based on the division of the available data into $k$ partitions, instantiating $k$ identical models, and training each one on $k - 1$ partitions while evaluating by using the remaining partition. The validation score for the model employed is then the average of the $k$ validation scores obtained (Chollet & Allaire, 2018). In this research $k = 5$ was considered.

### 6.2. Neural network architecture design

To avoid the loss of accuracy for any response when a multi output model is used (Chollet & Allaire, 2018), a different model was developed for each response (i.e. $g$ and $\varepsilon_{pc}$). Thus, in this research, two artificial neural network models were developed using R version 4.0.2 (2020-06-22) (R Core Team, 2018) by using the Keras package (Chollet & Allaire, 2018). The selection of hidden layers and hidden layer neurons is a trial and error process which frequently started by selecting a network with a minimum number of hidden layers and hidden neurons (Chandwani et al., 2015). For each response, different configurations were evaluated: one hidden layer, two hidden layers, and three hidden layers to achieve one optimal neural network architecture for $g$ and $\varepsilon_{pc}$. In each of these configurations, the number of neurons in each hidden layer ranged from 1 to 70 (about twice the amount of input data). Additionally, given the importance of the initial assignment of weights in the convergence of the learning algorithms, each architecture

**Table 8.** Parameters of artificial neural networks analysed in this research.

| Parameters of ANN models | | | |
|---|---|---|---|
| Type of neural network | Loss function | Activation function | Learning algorithm |
| Feed forward | Root mean squared error (RMSE) | *Relu* (rectified linear unit function) | RMSprop |

dealt with 100 different assignments of initial weights, selecting the allocation that produced the least error between the real and predicted values of the model in the first 100 epochs (number of times that the training data is passed through the artificial neural network during the adjusting process). In all these stages, the *k-fold* cross validation was used to assess the performance of the models. Once the architecture improvement has been selected for each configuration (number of hidden layers 1, 2 and 3), the selected models will be trained until epoch 2000. The chosen model for each response will be the one that offer the least error in *k- fold* cross-validation, having therefore selected the number of hidden layers, the number of neurons per layer, and the number of epochs required for training each of them (i.e. *g-model* and $\varepsilon_{pc}$*-model*).

Table 8 shows some of the characteristics common to all the network models tested in this research.

Regarding the concepts depicted in Table 8, a feed forward neural network is an artificial neural network wherein connections between the nodes do not form a cycle. In this network, the information moves in only one direction, forward, from the input nodes, through the hidden nodes and to the output nodes. The loss function takes the predictions of the network and the true target and computes a distance score, capturing how well the network has done on this specific example. It is used to enhance the model performance during the adjusting process. The activation function is the function that processes the signals inside each node and ascertains the model output. This function is what brings nonlinearity to the predictive model. Finally, the learning algorithm rules a step-by-step procedure for adjusting the connection weights of an artificial neural network. For further information about those neural network's concepts, some studies are listed in the references (Abellán-García, 2020c; Abellán-García, Fernández-Gómez, & Torres-Castellanos, 2020; Chollet & Allaire, 2018; Hudson Beale, 2012; Mushgil et al., 2015; Prasad et al., 2013).

### 6.3. Model performance evaluation

The artificial neural network models were trained on the training data by using the *k-fold* validation, and then the selected models' goodness was assessed on the test set. In this research, seven different statistical parameters have been used for measuring the model's predictive accuracy, viz., root mean square error (RSME), mean absolute error (MAE), average error (AE), coefficient of efficiency (E), root mean square error to the standard deviation of measured data ratio (RSR), normalised mean bias error (NMBE), and coefficients of multiple determination (R2), as indicated in Equations (3)–(9) respectively.

$$RMSE = \sqrt{\frac{\sum_{i=1}^{n}(a_i - \hat{a}_i)}{n}} \tag{3}$$

$$MAE = \frac{1}{n}\sum_{i=1}^{n}|a_i - \hat{a}_i| \tag{4}$$

$$AE = \frac{1}{n}\sum_{i=1}^{n}(a_i - \hat{a}_i) \tag{5}$$

$$E = 1 - \frac{\sum_{i=1}^{n}(a_i - \hat{a}_i)^2}{\sum_{i=1}^{n}(a_i - \overline{a}_i)^2} \tag{6}$$

$$RSR = \sqrt{\frac{RMSE}{\frac{1}{n}\sum_{i=1}^{n}(a_i - \overline{a}_i)^2}} \tag{7}$$

$$NMBE(\%) = \frac{\frac{1}{n}\sum_{i=1}^{n}(a_i - \hat{a}_i)}{\overline{a}_i} \times 100 \tag{8}$$

Table 9. Summary of results obtained for different configurations of neural network models.

| Response | Number of hidden layers | Best result (RMSE) | Model architecture |
|---|---|---|---|
| $g$ | 1 | 16.566 | 34-63-1 |
| | 2 | 14.112 | 34-62-45-1 |
| | 3 | 13.762 | 34-67-54-57-1 |
| $\varepsilon_{pc}$ | 1 | 0.1584 | 34-60-1 |
| | 2 | 0.1577 | 34-62-43-1 |
| | 3 | 0.1567 | 34-63-24-52-1 |

$$R^2 = 1 - \frac{\sum_{i=1}^{n}(a_i - \hat{a}_i)^2}{\sum_{i=1}^{n}(\hat{a}_i)^2} \tag{9}$$

where: $a$ represents the target or real value of the response; $\bar{a}$ is the mean of the target, $\hat{a}$ is the model's forecast and $n$ represents the total number of observations in the dataset.

RMSE is one of the most commonly employed error index statistics (Moriasi et al., 2007). RMSE measures the differences between the predicted values and the target values and computes the square root of the average residual error, pointing out the error in the units of the response. For a perfect fit, the optimal value of RMSE is zero. However, a weak point of this statistic would be that it provides more weightage to large errors (Chandwani et al., 2015). MAE is based on the absolute differences between the measured and the estimated; for a perfect fit the optimal value of MAE is zero (Abellán-García, 2020c). AE represents the average error; the smaller values of AE, the better performance of the model (Aderaw et al., 2018). The Nash Sutcliffe efficiency or coefficient of efficiency (E) (Nash & Sutcliffe, 1970) represents a ratio of residual error variance to contrasted variance in observed data; for a perfect association between the observed and predicted values the optimal value of E is 1. RSR was presented by (Moriasi et al., 2007); it incorporates the benefits of error index statistics and includes a normalization factor, thus, the resulting statistic and reported values can apply to various constituents. A lower value of RSR indicates a good performance of the model. NMBE supplies information on the mean bias in the estimations from a predictive model; a negative NMBE points out over-prediction while a positive NMBE points out under-prediction of the model (Srinivasulu & Jain, 2006). Coefficient of determination ($R^2$) compares the accuracy of the regression model with the accuracy of a surface benchmark model wherein the forecast is the average of all samples (Gupta, 2013); $R^2$ statistics is dependent on the linear relationships between the predicted and target values and may sometimes provide biased results when this relationship is not linear or when the values contain many outliers. For perfect association between the observed and predicted values, the perfect value of $R^2$ is 1. A combined use of the performance metrics can supply an unbiased estimate for prediction ability of the artificial neural network models.

## 7. Results and discussion

### 7.1. Artificial neural network models' architecture

Choosing the artificial neural network model architecture is the first important step in developing a model that best suits the problem at hand. Table 9 summarises the results obtained for the different configurations (number of hidden layers) measured by RMSE during the training using *k-fold* validation. It is important to highlight that Table 9 only depicts the best performing initial weight allocation of the neurons for each of the tested architectures during the first 100 epochs.

After selecting the best architectures for each number of hidden layers, the next step was to train each of these architectures during 2000 epochs. Figure 11 represents a smoothed curve of the measured error versus the number of epochs for each of these models.

There are three important issues to note in Figure 11. On the one hand, in both cases, the three hidden layer models outperformed the other models. On the other hand, according to this figure, validation RMSE stopped improving significantly after 261 and 273 epochs for g and $\varepsilon_{pc}$. Finally, there is a considerable enhancement in both models, going from a validation RSME of 13.762 to 10.344 in the case of $g$-model and from 0.1567 to 0.1149 in the case of $\varepsilon_{pc}$-model.

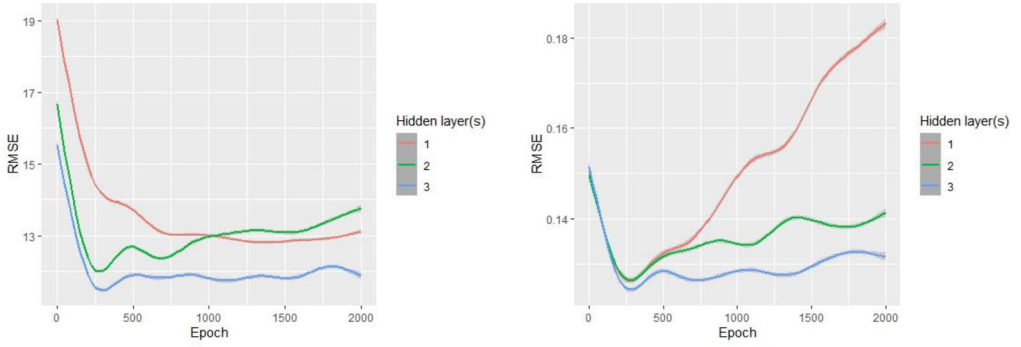


**Figure 11.** Smoothed curves of RMSE versus the number of epochs for each response: (a) energy capacity absorption, *g*; and the strain associated to the maximum post-cracking tensile strength - $\varepsilon_{pc}$.

Therefore, the selected model for *g* had 34 input nodes, 67 neurons in the first hidden layer, 54 neurons in the second hidden layer, 57 neurons in the third hidden layer, and one output (see Figure 12) and it was trained until epoch 261. Likewise, $\varepsilon_{pc}$-model had 34 input nodes, 63 neurons in the first hidden layer, 24 neurons in the second hidden layer, 52 neurons in the third hidden layer, and one output (see Figure 13) and in this case trained until epoch 261.

### 7.2. Performance evaluation of trained model

The results of the performance evaluation of the selected model are presented in Tables 10 and 11.

According to Tables 10 and 11, performance evaluation indicators have a similar value in training and test set. The latter indicates the proper performance of the *k-fold* validation utilised as methodology to avoid the overfitting of the artificial neural network model (Chollet & Allaire, 2018) during the training process. The proposed *g*-model predicted the energy capacity absorption on the test dataset with a RMSE value of 11.5488 and MAE value of 8.3143 kJ/m$^3$, pointing out that the differences between predicted and target values of compressive strength were relatively small. The model under-predicted the energy capacity absorption on average by $-0.2044$ kJ/m$^3$, according to the AE value resulted in the test set. E and RSR statistics, 0.7572 and 0.4828 respectively, confirmed the good performance of *g*-model. The NMBE statistic for training and testing was evaluated as 0.7477% and 0.0657%, showing the same sign which indicated both the consistency and under-prediction of the model. Finally, a $R^2$ value of 0.7581 was shown in the test data set. Moreover, Figure 14 clearly depicts that the predicted values were highly close to the corresponding target values.

In the case of the model to predict the maximum post-cracking strain ($\varepsilon_{pc}$), results depicted in Table 11 and Figure 15 exhibits the strong coherence between the predicted strain values and the real ones, achieving a RMSE, MAE, E, RSR and $R^2$ values of 0.1051, 0.0781, 0.7811, 0.4583 and 0.7924, respectively, in the test data set. In addition, NMBE and AE pointed out a slight under-prediction, as can be also observed in Figure 15b, where most of the points fell below the 45-graded line.

### 7.3. Discussion

As shown in Tables 10 and 12 and Figures 14 and 15, artificial neural network models present an accurate method for predicting the behaviour of UHPFRC under direct tensile test, even when blending up to two different types of fibres. The latter can be explained because of the immense ability of this artificial intelligence algorithms to map complex and nonlinear relationships between the inputs and the response. However, it can be observed that the $R^2$ values achieved for the *g* and $\varepsilon_{pc}$ prediction were smaller than those obtained by other authors consulted, who achieved higher correlation coefficients in the range between 0.96 and 0.98 when predicting the properties of UHPC/UHPFRC using neural networks

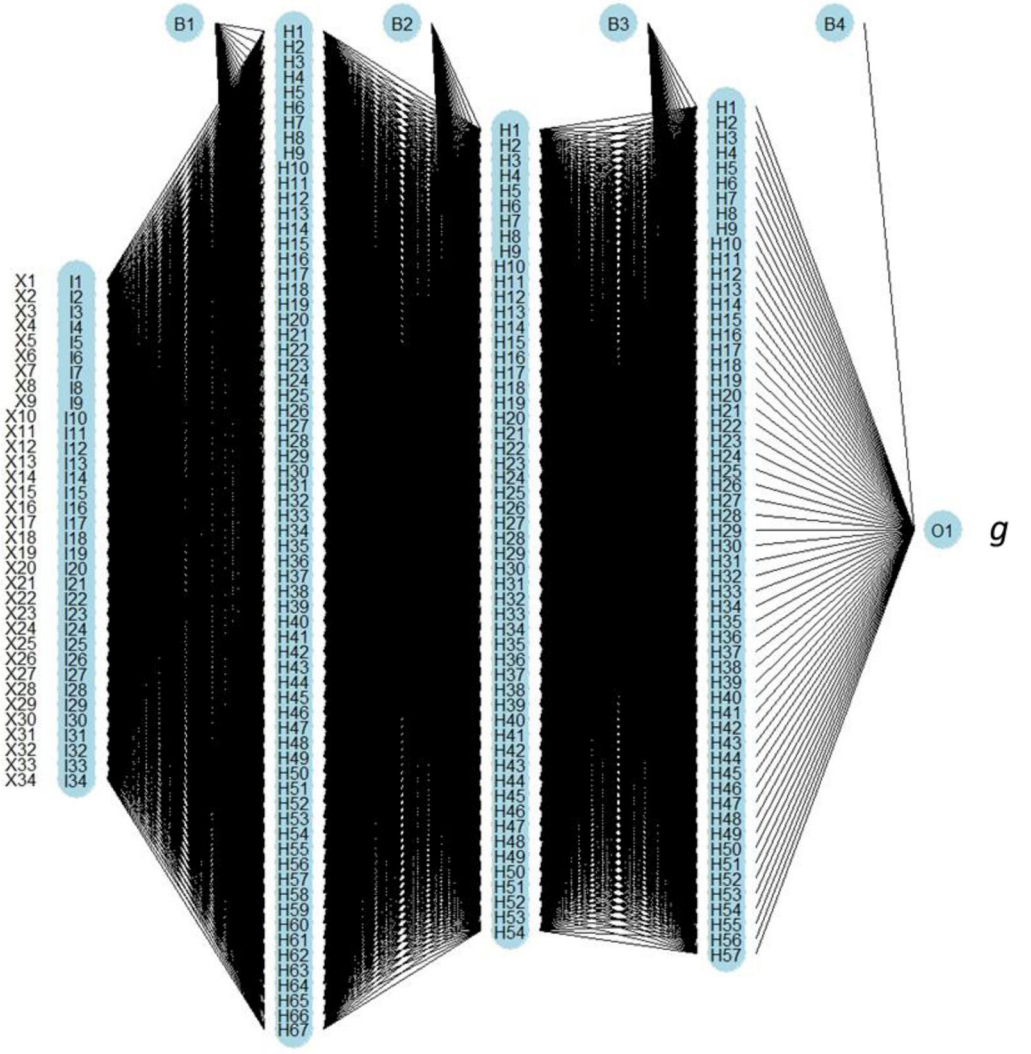


**Figure 12.** Artificial neural network model for predicting the energy capacity absorption of UHPFRC under direct tensile test *(g-model)*.

(Abellán-García et al., 2020; Ghafari et al., 2015; Zhang et al., 2017). This may be due to the fact that those references used only data from their own experimental work, limiting therefore the incorporation of statistical noise into the system, viz., the use of different types of cement and the characteristics of the supplementary cementitious materials such as physical and chemical properties, the unreported detail of the use of vibration during the pouring of the concrete, the different nature and shape of aggregates used in the database, and the different technology of superplasticizers considered in the database, among others.

On the other hand, other investigations that considered a mixture of their own data and data from the scientific literature obtained slightly better results than those presented here (Abellán-García, 2020; Abellán-García et al., 2020). In this case the differences may lay in the complexity of the tensile behaviour modelled here, in contrast to the compressive strength (Abellán-García, 2020) and flexural behaviour (Abellán-García et al., 2020) of UHPC/UHPFRC reported in those studies.

Finally, the good results obtained in the predictions of the direct tensile behaviour ($g$, $\varepsilon_{pc}$) on the experimental data (see Tables 10 and 11, and Figures 14b and 15b), encourage the authors to the next phase of the research: experimentally contrasted multi-objective optimisation.

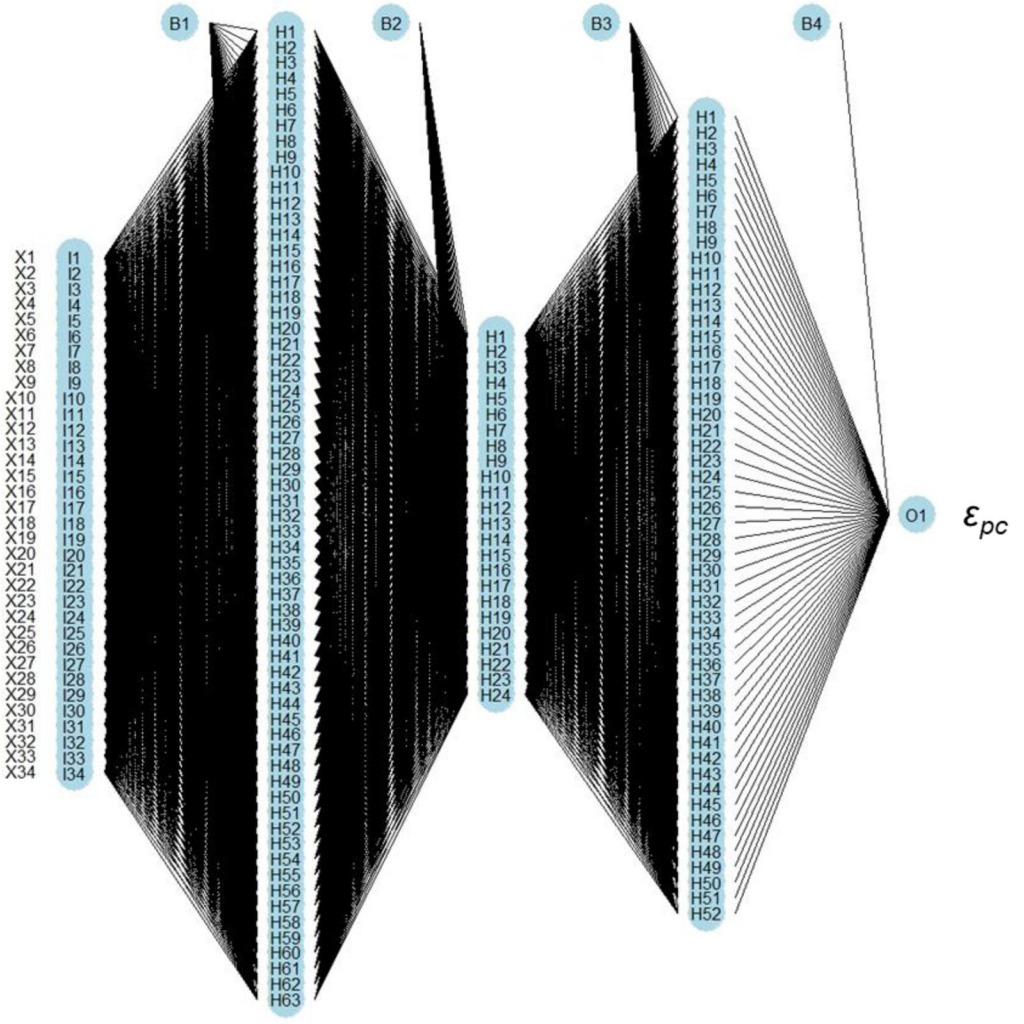


**Figure 13.** Artificial neural network model for predicting the strain associated to the maximum post-cracking tensile strength of UHPFRC under direct tensile test ($\varepsilon_{pc}$-model).

**Table 10.** *g*-Model performance measures.

| | Model performance | | | | | | |
|---|---|---|---|---|---|---|---|
| Data subset | RMSE | MAE | AE | E | RSR | NMBE (%) | $R^2$ |
| Training | 10.3340 | 7.1365 | 0.2217 | 0.7981 | 0.4388 | 0.7477 | 0.7997 |
| **Test** | **11.5488** | **8.3143** | **−0.2044** | **0.7572** | **0.4828** | **0.0657** | **0.7581** |
| Experimental | 5.9824 | 3.2952 | 0.0055 | 0.7394 | 0.5105 | 0.0821 | 0.7548 |

The neural netrwok models are trained with the training data subset but are evaluated with the test data subset.

**Table 11.** $\varepsilon_{pc}$-Model performance measures.

| | Model performance | | | | | | |
|---|---|---|---|---|---|---|---|
| Data subset | RMSE | MAE | AE | E | RSR | NMBE (%) | $R^2$ |
| Training | 0.1149 | 0.1070 | −0.0211 | 0.7899 | 0.4826 | 1.0410 | 0.7527 |
| **Test** | **0.1051** | **0.0781** | **0.0096** | **0.7811** | **0.4583** | **1.4966** | **0.7924** |
| Experimental | 0.0602 | 0.0431 | −0.0380 | 0.3320 | 0.8173 | 0.3012 | 0.7427 |

The neural netrwok models are trained with the training data subset but are evaluated with the test data subset.

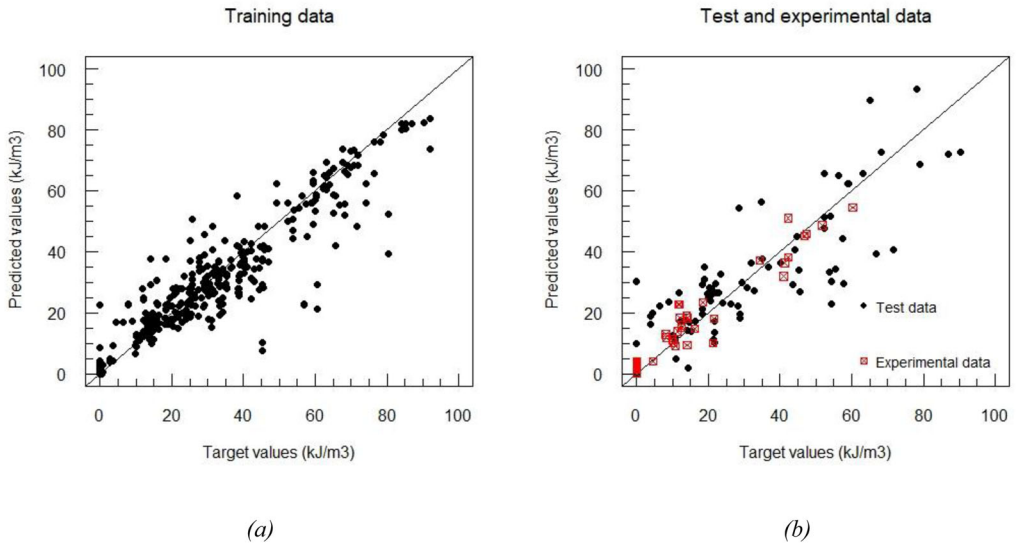


**Figure 14.** Regression plot for *g*-model: (a) training data; (b) experimental and test data.

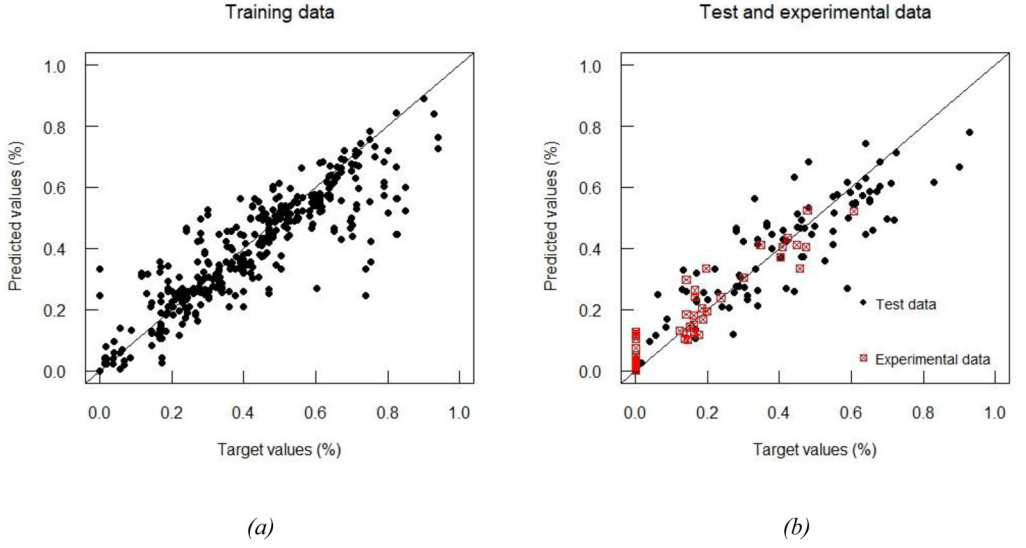


**Figure 15.** Regression plot for $\varepsilon_{pc}$-model: (a) training data; (b) experimental and test data.

**Table 12.** Optimisation of the individual responses for a UHPFRC mixture for seismic retrofitting applications with locally available materials (fibres) at lower cost.

| Responses and variables | Lower | Upper | Goal | Importance |
|---|---|---|---|---|
| $g$ (kJ/m$^3$) | 50 | 75 | Maximum | 5 |
| $\varepsilon_{pc}$ (%) | 0.3 | 0.5 | Maximum | 5 |
| Cost (×1,000 COP)[a] | 500 | 2,000 | Minimum | 5 |

a×1,000 Colombian pesos.

Table 13. Optimum fibre combination for seismic retrofitting applications.

| Fibre 1 | | Fibre 2 | | | | | |
|---|---|---|---|---|---|---|---|
| Notation | Volume (%) | Notation | Volume (%) | Total volume (%) | $g$ (kJ/m$^3$) | $\varepsilon_{pc}$ (%) | Cost (×1,000 COP) |
| $S_1$ | 0.340 | $H_2$ | 1.360 | 1.700 | 50.448 | 0.424 | 811.910 |

## 8. Multi-objective optimisation

### 8.1. Methodology

A multi-objective optimisation R-coded algorithm (Roth, 2016) was employed, aimed at settling the optimum values for the input variables (fibres properties only in this case) that can reach the best value for the response. Once the artificial neural networks models were selected, inputs variable corresponding to the fibres (i.e. from X10 to X33, both included) were assigned simultaneously and independently to enhance the best trade-off of the objective functions without excessively compromising any of the requirements (Abellán et al., 2020; Abellán-García et al., 2020; Ghafari et al., 2014; Ghafari, Costa, & Júlio, 2015) by considering the commercially available fibres in Colombia depicted in Table 7. The input variables corresponding to the cementitious matrix (i.e. from X1 to X9 plus X34) were fixed to the values of the optimised mixture shown in Table 5 (Abellán et al., 2020).

The optimisation R-coded algorithm used in this study was based on the desirabilities approach developed by Derringer & Suich (Derringer & Suich, 1980), where the predicted values of each response variables are transformed into values within the interval [0.1] using three different desirability methods for the three different optimisation criteria (i.e. minimise, maximise, in range). Each value of a response variable can be assigned a specific desirability, optimising more than one response variable.

Derringer & Suich (Derringer & Suich, 1980) defined the desirability cases of minimisation, maximisation, and in range individual responses, as in Equations (10), (11) and (12), respectively.

$$d = \begin{cases} 1 & Y_i \le L \\ \left[\frac{U-Y_i}{U-L}\right]^{wt_i} & L<Y_i<U \\ 0 & Y_i \ge U \end{cases} \tag{10}$$

$$d = \begin{cases} 0 & Y_i \le L \\ \left[\frac{Y_i-L}{U-L}\right]^{wt_i} & L<Y_i<U \\ 1 & Y_i \ge U \end{cases} \tag{11}$$

$$d = \begin{cases} 0 & Y_i \le L \\ 1 & L<Y_i<U \\ 0 & Y_i \ge U \end{cases} \tag{12}$$

There are several ways to draw the optimal solution considering multiple individual desirability functions, but the most widely used method is to optimise by converting multiple desirability functions into single desirability D (Derringer & Suich, 1980; Ghafari et al., 2014; Ghafari, Costa, & Júlio, 2015). The geometric mean of the specific desirabilities characterises the overall desirability as follows in Equation (13):

$$D = \left(d_1^{r_1} \times d_2^{r_2} \times d_3^{r_3} \times \cdots \times d_n^{r_n}\right)^{1/\sum r_i} = \left[\prod_{i=1}^{n} d_i^{r_n}\right]^{1/\sum r_i} \tag{13}$$

A value of D different from zero in Equation (13) implies that all responses are in a desirable range simultaneously and, consequently, for a value of D close to 1, the combination of the different criteria is globally optimum, so the response values are near their target values. However, if any of the responses fall outside their desirability range, the overall function becomes zero. In Equation (13), $r_i$ represents the relative importance assigned to the response $i$. The relative importance $r_i$ is a comparative scale for weighting of each individual desirability functions ($d_i$) in the overall desirability product and it varies from least important ($r_i = 1$) to most important ($r_i = 5$). It is important to point out that the outcome of the overall desirability D depends on the $r_i$ value that offers users flexibility in the definition of desirability functions. In this study, shape constants equal 5 in all cases.

The goals of the criteria optimisation for each response are shown in Table 12. It has been proposed to select the optimum mix design variables for obtaining a UHPFRC with the proper characteristics to be

Table 14. Forecasted responses by model versus experimental values.

| $g$ (kJ/m$^3$) | | | $\varepsilon_{pc}$ (%) | | |
|---|---|---|---|---|---|
| Experimental | Model | Deviation (%) | Experimental | Model | Deviation (%) |
| 45.177 | 50.448 | 11.667 | 0.458 | 0.424 | 7.424 |

Figure 16. Multi-cracking pattern in the experimental validation specimen gage.

used as seismic retrofitting of existing non-ductile concrete structure, i.e. $g \geq 50$ kJ/m$^3$ and $\varepsilon_{pc} \geq 0.3\%$, at lower costs. At the end of the multi-objective optimisation process, one optimal solution satisfying the specified constraints was obtained. The optimised mixture is presented in Table 13.

### 8.2. Validation of the multi-objective optimisation

The efficiency of the designed model was evaluated by carrying out the experiment with the selected value fibre blending and by comparing experimental measured values obtained with those indicate by the mathematical model. The mixture of fibres selected by the multi-objective algorithm is presented in Table 13. The comparison between theoretical and experimental results is shown in Table 14. The percentual deviation was employed as a measure of accuracy for validation. Results confirmed that the experimental values agree with the values predicted by the proposed model.

It is important to note that even the experimental value for $g$ was inferior to the proposed limit, the value is remarkably close to 50 kJ/m$^3$. Furthermore, several researches have insisted in considering $g$ as the area under the stress–strain curve up to $\sigma_u$ ( 95% of $\sigma_{pc}$ on the descending branch (Pyo et al., 2016; Abellán-García et al., 2021). Considering this criterion, the value of $g$ obtained in the experimental value would be 67.830 kJ/m$^3$, value that satisfies the necessary level of ductility for earthquake resistant applications (Dogan & Krstulovic-Opara, 2003; Lavorato et al., 2017; Massicotte et al., 2013; Vasconez et al., 1998).

Figure 16 depicts the multi-cracking phenomenon in the experimental verification.

## 9. Conclusions

In this paper, two accurate artificial neural network models were developed to predict tensile behaviour of UHPFRC when using up to two different types of fibres as reinforcement. To avoid overfitting, *k-fold* validation with five partitions was employed, thereby leading to higher confidence of the models when predicting on new data. Focus was made in achieving the ductility for seismic retrofitting applications by using a multi-objective simultaneous optimisation algorithm. From the obtained results of this research, the following conclusions are drawn:

1. The proposed models based on a wide range of experimental and previous work data can be very handy for forecasting the tensile behaviour of UHPFRC promptly. It could be helpful in the developing of UHFRPC for seismic retrofitting applications. This mathematical tool will considerably decrease the effort, costs, and time to design an UHPFRC dosage for the necessary ductility (i.e. $g \geq 50$ kJ/m$^3$

and $\varepsilon_{pc} \geq 0.3\%$ under direct tensile test) when dealing with locally available materials and fibres without performing multiple trials.
2. The selected models for predicting the energy capacity absorption (g) and the strain corresponding to the maximum post-cracking strength under direct tensile test ($\varepsilon_{pc}$) were composed by three hidden layers each, with architectures of 34-67-54-57-1 and 34-63-24-52-1, respectively.
3. The results of the combined use of the performance metrics, which included RMSE, MAE, AE, E, RSR, NMBE, $R^2$, supplied an unbiased estimate which proved the adequacy of the proposed artificial neural networks models for such a complex phenomenon like the tensile behaviour of UHPFRC.
4. The optimal blending of fibres for achieving the necessary properties for seismic retrofitting applications when using a previously optimised UPHC mixture was 0.34% of high-strength steel straight ($l_f/d_f = 65$) fibres in addition to 1.36% of normal strength hooked end steel fibres ($l_f/d_f = 80$). Totalising a total volume fibre fraction on 1.7%.

Finally, this report demonstrated that it is possible to achieve a UHPFRC with the necessary ductility for seismic retrofitting applications when using low fibre content and an innovative optimized cementitious matrix under sustainability criteria by incorporating green materials in partial replacement of cement and silica fume.

## Disclosure statement

No potential conflict of interest was reported by the authors.

## References

Abbas, S., Nehdi, M. L., & Saleem, M. A. (2016). Ultra-high performance concrete: Mechanical performance, durability, sustainability and implementation challenges. *International Journal of Concrete Structures and Materials*, *10*(3), 271–295. https://doi.org/10.1007/s40069-016-0157-4

Abdulkareem, O. M., Ben Fraj, A., Bouasker, M., & Khelidj, A. (2018). Effect of chemical and thermal activation on the microstructural and mechanical properties of more sustainable UHPC. *Construction and Building Materials*, *169*, 567–577. https://doi.org/10.1016/j.conbuildmat.2018.02.214

Abellán, J., Fernández, J., Torres, N., & Núñez, A. (2020a). Development of cost-efficient UHPC with local materials in Colombia. In *Proceedings of Hipermat 2020 - 5th International Symposium on UHPC and Nanotechnology Construction Materials* (pp. 97–98). Kassel University Press.

Abellán, J., Fernández, J., Torres, N., & Núñez, A. (2020b). Statistical optimization of ultra-high-performance glass concrete. *ACI Materials Journal*, *117*, 243–254. https://doi.org/10.14359/51720292

Abellán, J., Núñez, A., & Arango, S. (2020). Pedestrian bridge of UNAL in Manizales: A new UPHFRC application in the Colombian building market. In: *Proceedings of Hipermat 2020 - 5th International Symposium on UHPC Nanotechnology Construction* (pp. 43–44). Kassel University Press.

Abellan, J., Torres, N., Núñez, A., & Fernández, J. (2018). Ultra high preformance fiber reinforced concrete: State of the art, applications and possibilities into the Latin American market. In: *XXXVIII Jornadas Sudamericanas de Ingenieria Estructural*, Lima, Perú.

Abellan, J., Torres, N., Núñez, A., & Fernández, J. (2018). Influencia del exponente de Fuller, la relación agua conglomerante y el contenido en policarboxilato en concretos de muy altas prestaciones, In: IV Congr. Int. Ing. Civ., Havana, Cuba.

Abellán-García, J. (2020a). Comparison of artificial intelligence and multivariate regression in modeling the flexural behavior of UHPFRC. *Dyna*, *87*, 239–248. https://doi.org/10.15446/dyna.v87n214.86172.

Abellán-García, J. (2020b). *Dosage optimization and seismic retrofitting applications of Ultra-HighPerformance Fiber Reinforced Concrete (UHPFRC)*. PhD Thesis. Universidad Politécnica de Madrid.

Abellán-García, J. (2020c). Four-layer perceptron approach for strength prediction of UHPC. *Construction and Building Materials*, *256*, 119465. https://doi.org/10.1016/j.conbuildmat.2020.119465

Abellán-García, J. (2021). K-fold validation neural network approach for predicting the one-day compressive strength of UHPC. *Advances in Civil Engineering Materials*, *10*(1), 20200055. https://doi.org/10.1520/ACEM20200055

Abellán-García, J., Fernández-Gómez, J. A., Torres-Castellanos, N., & Núñez-López, A. M. (2020). Machine learning prediction of flexural behavior of UHPFRC. In P. Serna, A. Llano-Torre, J. R. Martí-Vargas, & J. Navarro-Gregori (Eds.), *Fibre Reinforced Concrete: Improvements and Innovations. BEFIB 2020, RILEM Bookseries* (pp. 570–583). Springer Nature Switzerland AG https://doi.org/10.1007/978-3-030-58482-5_52 .

Abellán-García, J., Fernández-Gómez, J., & Torres-Castellanos, N. (2020). Properties prediction of environmentally friendly ultra-high-performance concrete using artificial neural networks. *European Journal of Environmental and Civil Engineering*, 1–25. https://doi.org/10.1080/19648189.2020.1762749

Abellán-García, J., Fernández-Gómez, J., Torres-Castellanos, N., & Núñez-López, A. (2021). Tensile behavior of normal strength steel fiber green UHPFRC. *ACI Materials Journal*, *118*, 127–138. https://doi.org/10.14359/51725992

Abellán-García, J., & Guzmán-Guzmán, J. S. (2021). Random forest-based optimization of UHPFRC under ductility requirements for seismic retrofitting applications. *Construction and Building Materials*, *285*, 122869. https://doi.org/10.1016/j.conbuildmat.2021.122869

Abellán-García, J., Guzmán-Guzmán, J. S., Sánchez-Díaz, J. A., & Rojas-Grillo, J. (2021). Experimental validation of artificial intelligence model for the energy absorption capacity of UHPFRC. *Dyna*, *88*, 150–159. https://doi.org/10.15446/dyna.v88n217.

Abellán-García, J., Nuñez-Lopez, A., & Arango-Campo, S. (2020). Pedestrian bridge over Las Vegas Avenue in Medellín. First Latin American infrastructure in UHPFRC. In P. Serna, A. Llano-Torre, J. R. Martí-Vargas, & J. Navarro-Gregori (Eds.), Fiber Reinforced Concrete: Omprovements and Innovations, *BEFIB 2020, RILEM Bookseries* (pp. 864–872). Springer Nature Switzerland AG. https://doi.org/10.1007/978-3-030-58482-5_76.

Abellán-García, J., Núñez-López, A., Torres-Castellanos, N., & Fernández-Gómez, J. (2019). Effect of FC3R on the properties of ultra-high-performance concrete with recycled glass. *Dyna*, *86*, 84–92. https://doi.org/10.15446/dyna.v86n211.79596

Abellán-García, J., Núñez-López, A., Torres-Castellanos, N., & Fernández-Gómez, J. (2020). Factorial design of reactive powder concrete containing electric arc slag furnace and recycled glass powder. *Dyna*, *87*, 42–51. https://doi.org/10.15446/dyna.v87n213.82655.

Abellan-Garcia, J., Santofimo-Vargas, M. A., & Torres-Castellanos, N. (2020). Analysis of metakaolin as partial substitution of ordinary Portland cement in Reactive Powder Concrete. *Advances in Civil Engineering Matrials*, *9*, 368–386. https://doi.org/10.1520/ACEM20190224

Abellán-García, J., Torres-Castellanos, N., Fernández-Gómez, J. A., & Núñez-López, A. M. (2021). Ultra-high-performance concrete with local high unburned carbon fly ash. *Dyna*, *88*, 38–47. https://doi.org/10.15446/dyna.v88n216.89234.

ACI Committe 239R, (2018). ACI – 239 Committee in Ultra-High Performance Concrete, ACI, Toronto.

Acker, P., & Behloul, M. (2004). Ductal technology: A large spectrum of properties, a wide range of applications. In: M. Fröhlich & S. Piotrowski (Eds.), *Proc. Int. Symp. Ultra High Perform. Concr.* (pp. 11–24). Kassel University.

Adeli, H. (2001). Neural networks in civil engineering: 1989 — 2000. *Computer-Aided Civil and Infrastructure Engineering*, *16*(2), 126–142. https://doi.org/10.1111/0885-9507.00219

Aderaw, M., Muse, S., & Abiero, Z. C. (2018). Artificial neural network based modelling approach for strength prediction of concrete incorporating agricultural and construction wastes. *Construction and Building Materials*, *190*, 517–525. https://doi.org/10.1016/j.conbuildmat.2018.09.097

AlHallaq, A. F., Tayeh, B. A., & Shihada, S. (2017). Investigation of the bond strength between existing concrete substrate and UHPC as a repair material. *International Journal of Engineering and Advanced Technology*, *6*, 210–217.

Asociación Colombiana de Ingeniería Sísmica (2010). Reglamento Colombiano de construcciónsismo resistente. NSR-10. Asociación Colombiana de Ingeniería.

Atkinson, A., & Riani, M. (2000). *Robust diagnostic regression analysis*. Springer US.

Bracci, J. M., Reinhorn, A. M., & Mander, J. B. (1955). Seismic resistance of reinforced concrete frame structures designed for gravity loads: Performance of structural system. *ACI Structural Journal*, *92*(5), 597–609.

Byars, E. A., Waldron, P., Dejke, V., & Demis, S. (2001). *Durability of FRP in concrete current specifications and a new approach*. FRP Compos.

Centro de Estudios e Investigaciones Sobre Riesgo. (2005). *Escenarios de riesgo y pérdidas por terremoto para Bogotá*. University of Los Andes.

Chandwani, V., Agrawal, V., & Nagar, R. (2014). Applications of artificial neural networks in modeling compressive strength of concrete: A state of the art review. *Advances in Artificial Neural Systems*, *2014*, 1–2956. https://doi.org/10.1155/2014/629137

Chandwani, V., Agrawal, V., & Nagar, R. (2015). Modeling slump of ready mix concrete using genetic algorithms assisted training of artificial neural networks. *Expert Systems with Applications*, *42*(2), 885–893. https://doi.org/10.1016/j.eswa.2014.08.048

Chao, S. (2016). Seismic behavior of ultra-high-performance fiber-reinforced concrete moment frame members [Paper presentation]. International Interactive Symposium on UHPC (pp. 1–10). TOCIEJ-13-147

Chollet, F., & Allaire, J. J. (2018). *Deep learning with R*. Manning Publications Co.

Dagenais, M. A., Massicotte, B., & Boucher-Proulx, G. (2018). Seismic retrofitting of rectangular bridge piers with deficient lap splices using ultrahigh-performance fiber-reinforced concrete. *Journal of Bridge Engineering*, *23*, 1–13. https://doi.org/10.1061/(ASCE)BE.1943-5592.0001173

De Domenico, D., Impollonia, N., & Ricciardi, G. (2019). Seismic retrofitting of confined masonry-RC buildings: The case study of the university hall of residence in Messina, Italy. *Ingeniería Sísmica*, *36*, 54–85.

De Larrard, F. (1999). Concrete mixture proportioning: A scientific approach. (1st ed.). CRC Press. https://doi.org/10.1201/9781482272055

De Larrard, F., & Sedran, T. (2002). Mixture-proportioning of high-performance concrete. *Cement and Concrete Research*, *32*(11), 1699–1704. https://doi.org/10.1016/S0008-8846(02)00861-X

Derringer, G., & Suich, R. (1980). Simultaneous optimization of several response variables. *Journal of Quality Technology*, *12*(4), 214–219. https://doi.org/10.1080/00224065.1980.11980968

Dogan, E., & Krstulovic-Opara, N. (2003). Seismic retrofit with continuous slurry-infiltrated mat concrete jackets. *ACI Structural Journal*, *100, 713-722*.

Estebon, M. D. (1997). *Perceptrons: An associative learning network*. Virginia Tech.

Everitt, B., & Hothorn, T. (2015). MVA: An introduction to applied multivariate analysis with R. Springer.

Funk, J. E. J. E., & Dinger, D. R. (1994). *Predictive process control of crowded particulate suspensions: Applied to ceramic manufacturing*. Springer Science. https://doi.org/10.1007/978-1-4615-3118-0

Garcia, L. E. (2014). Desarrollo de la normativa sismo resistente colombiana en los 30 años desde su primera expedición. *Revista de Ingeniería*, *41*, 71–77.

Ghafari, E. (2012). *Optimization of UHPC by adding nanomaterials*. In Proceedings of Hipermat 2012, 3rd Int. Symp. UHPC Nanotechnol. Constr. Mater., Kassel Uni, Kassel, Alemania (pp. 71–78).

Ghafari, E., Bandarabadi, M., Costa, H., & Júlio, E. (2015). Prediction of fresh and hardened state properties of UHPC: Comparative study of statistical mixture design and an artificial neural network model. *Journal of Materials in Civil Engineering*, *27*(11), 04015017. https://doi.org/10.1061/(ASCE)MT.1943-5533.0001270

Ghafari, E., Costa, H., & Júlio, E. (2015). Statistical mixture design approach for eco-efficient UHPC. *Cement and Concrete Composites*, *55*, 17–25. https://doi.org/10.1016/j.cemconcomp.2014.07.016

Ghafari, E., Costa, H., Júlio, E., Portugal, A., & Durães, L. (2012). Enhanced durability of ultra high performance concrete by incorporating supplementary cementitious materials. In *Second Int. Conf. Microstruct.* Durab. Cem. Compos (pp. 11–13).

Ghafari, E., Costa, H., Nuno, E., & Santos, B. (2014). RSM-based model to predict the performance of self-compacting UHPC reinforced with hybrid steel micro-fibers. *Construction and Building Materials*, *66*, 375–383. https://doi.org/10.1016/j.conbuildmat.2014.05.064

Ghafari, E., Costa, H., Nuno, E., Santos, B., Costa, H., & Júlio, E. (2015). Critical review on eco-efficient ultra high performance concrete enhanced with nano- materials. *Construction and Building Materials*, *101*, 201–208. https://doi.org/10.1016/j.conbuildmat.2015.10.066

Gupta, S. (2013). Using artificial neural network to predict the compressive strength of concrete containing nano-silica. *Civil Engineering and Architecture*, *1*(3), 96–102. https://doi.org/10.13189/cea.2013.010306

Haber, Z. B., Munoz, J. F., & Graybeal, B. A. (2017). Field testing of an ultra-high performance concrete overlay. Technical Report. U.S. Department of Transportation. Federal Highway Administration.

Härdle, W. K., & Simar, L. (2012). *Applied multivariate statistical analysis*. Springer-Verlag GmbH.

Hudson Beale, M. (2012). *Neural network toolbox user's guide*. MathWorks J.

Kalny, M., Kvasnicka, V., & Komanec, J. (2016). First practical applications of UHPC in the Czech Republic. In E. Fehling, B. Middendorf, & J. Thiemicke (Eds.), *Proc. Hipermat 2016 - 4th Int. Symp. UHPC Nanotechnol. Constr. Mater.* (pp. 147–148). Kassel.

Khan, M. I., Al-Osta, M. A., Ahmad, S., & Rahman, M. K. (2018). Seismic behavior of beam-column joints strengthened with ultra-high performance fiber reinforced concrete. *Composite Structures*, *200*, 103–119. https://doi.org/10.1016/j.compstruct.2018.05.080

Khashman, A., & Akpinar, P. (2017). ScienceDirect non-destructive prediction of concrete compressive strength using neural networks prediction of concrete compressive strength using neural networks. *Procedia Computer Science*, *108*, 2358–2362. https://doi.org/10.1016/j.procs.2017.05.039

Kim, D.-J., Naaman, A. E., & El-Tawil, S. (2009). High performance fiber reinforced cement composites with innovative slip hardending twisted steel fibers. *International Journal of Concrete Structures and Materials*, *3*(2), 119–126. https://doi.org/10.4334/IJCSM.2009.3.2.119

Kim, D. J., Park, S. H., Ryu, G. S., & Koh, K. T. (2011). Comparative flexural behavior of hybrid ultra high performance fiber reinforced concrete with different macro fibers. *Construction and Building Materials*, *25*(11), 4144–4155. https://doi.org/10.1016/j.conbuildmat.2011.04.051

Kou, S. C., & Xing, F. (2012). The effect of recycled glass powder and reject fly ash on the mechanical properties of fibre-reinforced ultrahigh performance concrete, hindawi publ. *Advances in Materials Science and Engineering*, *2012*, 1–8. https://doi.org/10.1155/2012/263243

Kwon, S., Nishiwaki, T., Kikuta, T., & Mihashi, H. (2014). Development of ultra-high-performance hybrid fiber-reinforced cement-based composites. *ACI Materials Journal*, *111*, 309–318. https://doi.org/10.14359/51686890

Larrard, F. (1994). Optimization of ultra-high performance concrete by the use of a packing model. *Cement and Concrete Research*, *24*, 997–1009.

Lavorato, D., Bergami, A. V., Nuti, C., Briseghella, B., Xue, J., Tarantino, A. M., Marano, G. C., & Santini, S. (2017). *Ultra-high-performance fibre-reinforced concrete jacket for the repair and the seismic retrofitting of Italian and Chinese RC bridges* [Paper presentation]. COMPDYN 2017 - Proc. 6th Int. Conf. Comput. Methods Struct. Dyn. Earthq. Eng. (Vol. 1, pp. 2149–2160). Eccomas Proceedia. https://doi.org/10.7712/120117.5556.18147.

Martin-Sanz, H., Chatzi, E., & Brühwiler, E. (2016). The use of ultra high performance fibre reinforced cement-based composites in rehabilitation projects: A review.[Paper presentation] In V. Saouma, J. Bolander, & E. Landis (Eds.), *9th International Conference on Fracture Mechanics of Concrete and Concrete Structures*. https://doi.org/10.21012/fc9.219

Massicotte, B., Dagenais, M.-A., & Lagier, F. (2013). *Performance of UHPFRC jackets for the seismic strengthening of bridge piers*. RILEM-Fib-AFGC Int. Symp. Ultra-High Perform. Fibre-Reinforced (pp. 89–98). Springer.

Moriasi, D. N., Arnold, J. G., Liew, M. W V., Bingner, R. L., Harmel, R. D., & Veith, T. L. (2007). Model evaluation guidelines for systematic quantification of accuracy in watershed in simulations. *American Society of Agricultural and Biological Engineers*, *50*, 885–900.

Mushgil, H. M., Alani, H. A., & George, L. E. (2015). Comparison between resilient and standard back propagation algorithms efficiency in pattern recognition. *International Journal of Scientific and Engineering Research*, *6*, 773–778.

Naaman, A. E., & Reinhardt, H. W. (2007). Proposed classification of HPFRC composites based on their tensile response. *Materials and Structures*, *39*(5), 547–555. https://doi.org/10.1617/s11527-006-9103-2

Nash, E., & Sutcliffe, V. (1970). River flow forecasting through conceptual models. Part I - A discussion of principles. *Journal of Hydrology*, *10*(3), 282–290. https://doi.org/10.1016/0022-1694(70)90255-6

Park, S. H., Kim, D. J., Ryu, G. S., & Koh, K. T. (2012). Tensile behavior of ultra high performance hybrid fiber reinforced concrete. *Cement and Concrete Composites*, *34*(2), 172–184. https://doi.org/10.1016/j.cemconcomp.2011.09.009

Parra-Montesinos, G., & Wight, J. K. (2000). Seismic behavior, strength and retrofit of RC column-to-steel beam connections. nisee.berkeley.edu. *Retrieved from http://nisee.berkeley.edu/elibrary/Text/S37269*

Prasad, N., Singh, R., & Lal, S. P. (2013). *Comparison of back propagation and resilient propagation algorithm for spam classification* [Paper presentation]. Proc. Int. Conf. Comput. Intell. Model. Simul. (pp. 29–34). https://doi.org/10.1109/CIMSim.2013.14. IEEE.

Pyo, S., El-Tawil, S., & Naaman, A. E. (2016). Direct tensile behavior of ultra high performance fiber reinforced concrete (UHP-FRC) at high strain rates. *Cement and Concrete Research*, *88*, 144–156. https://doi.org/10.1016/j.cemconres.2016.07.003

R Core Team. (2018). *R: A language and environment for statistical computing*. https://www.r-project.org/.

Richard, P., & Cheyrezy, M. (1995). Composition of reactive powder concretes. *Cement and Concrete Research*, *25*(7), 1501–1511. https://doi.org/10.1016/0008-8846(95)00144-2

Rosenblatt, F. (1958). The perceptron: A probabilistic model for information storage and organization in the brain. *Psychological Review*, *65*(6), 386–408. https://doi.org/10.1037/h0042519

Roth, T. (2016). *Working with the quality tools package*, 35. http://www.r-qualitytools.org.

Ruiz-Pinilla, J. C., Pallarés, F. J., Gimenez, E., & Calderón, P. A. (2014). Experimental tests on retrofitted RC beam-column joints underdesigned to seismic loads. *Engineering Structures*, *59*, 702–714. https://doi.org/10.1016/j.engstruct.2013.11.008

Ryu, G. S., Kim, S. H., Ahn, G. H., & Koh, K. T. (2012). Evaluation of the direct tensile behavioral characteristics of UHPC using twisted steel fibers. *Advanced Materials Research*, *602–604*, 96–101. https://doi.org/10.4028/www.scientific.net/AMR.602-604.96

Schmidt, C., & Schmidt, M. (2012). Whitetopping' of asphalt and concrete pavements with thin layers of ultra-high-performance concrete - Construction and economic efficiency. In: M. Fröhlich & S. Piotrowski (Eds.), *3rd Int. Symp. UHPC Nanotechnol. High Perform. Constr. Mater.* (pp. 921–927). Kassel University.

Shaaban, M., & Ahmed, S. (2016). Development of ultra-high performance concrete jointed precast decks and concrete piles in integral abutment bridges. In First Int. Symp. Jointless Sustain. Bridg., Fujian, China. https://www.academia.edu/25363851/development_of_ultra-high_performance_concrete_for_jointed_precast_decks_and_concrete_piles_in_integral_abutment_bridges.

Soliman, N. A., & Tagnit-Hamou, A. (2017a). Partial substitution of silica fume with fine glass powder in UHPC: Filling the micro gap. *Construction and Building Materials*, *139*, 374–383. https://doi.org/10.1016/j.conbuildmat.2017.02.084

Soliman, N. A., & Tagnit-Hamou, A. (2017b). Using glass sand as an alternative for quartz sand in UHPC. *Construction and Building Materials*, *145*, 243–252. https://doi.org/10.1016/j.conbuildmat.2017.03.187

Soliman, N. A., & Tagnit-Hamou, A. (2017c). Using particle packing and statistical approach to optimize eco-efficient ultra-high-performance concrete. *ACI Materials Journal*, *114*, 847–858. https://doi.org/10.14359/51701001

Soranakom, C., & Mobasher, B. (2008). Correlation of tensile and flexural responses of strain softening and strain hardening cement composites. *Cement Concr. Compos*. 30(6), 465–477. https://doi.org/10.1016/j.cemconcomp.2008.01.007

Srinivasulu, S., & Jain, A. (2006). A comparative analysis of training methods for artificial neural network rainfall – runoff models. *Applied Soft Computing*, *6*(3), 295–306. https://doi.org/10.1016/j.asoc.2005.02.002

Taghaddos, H., Mahmoudzadeh, F., Pourmoghaddam, A., & Shekarchizadeh, M. (2004). Prediction of compressive strength behaviour in RPC with applying an adaptive network-based fuzzy interface system. In: *Proc. Int. Symp. Ultra High Perform* (pp. 273–284). Kassel University Press.

Tagnit-Hamou, A., Soliman, N. A., & Omran, A. (2016). Green ultra - high - performance glass concrete. *First Int. Interact. Symp. UHPC – 2016*, *3*, 1–10.

Tayeh, B. A., Abu Bakar, B. H., Megat Johari, M. A., & Voo, Y. L. (2013). Utilization of ultra-high performance fibre concrete (UHPFC) for rehabilitation - A review. *Procedia Engineering*, *54*, 525–538. https://doi.org/10.1016/j.proeng.2013.03.048

Van Tuan, N., Ye, G., van Breugel, K., Fraaij, A. L. A., & Bui, D. D. (2011). The study of using rice husk ash to produce ultra high performance concrete. *Construction and Building Materials*, *25*(4), 2030–2035. https://doi.org/10.1016/j.conbuildmat.2010.11.046

Vasconez, R. M., Naaman, A. E., & Wight, J. K. (1998). Behavior of HPFRC connections for precast concrete frames under reversed cyclic loading. *PCI Journal*, *43*(6), 58–71. https://doi.org/10.15554/pcij.11011998.58.71

Vega Vargas, C. J. (2015). *Comportamiento dinámico de muros de mampostería no estructural reforzados mediante polímeros reforzados con fibra de carbono*. CFRP, Escuela Colombiana de Ingeniería Julio Garavito.

Wille, K., El-Tawil, S., & Naaman, A. E. (2014). Properties of strain hardening ultra high performance fiber reinforced concrete (UHP-FRC ) under direct tensile loading. *Cement and Concrete Composites*, *48*, 53–66. https://doi.org/10.1016/j.cemconcomp.2013.12.015

Wille, K., Kim, D., & Naaman, A. E. (2011). Strain hardening UHP-FRC with low fiber contents. *Materials and Structures 44*, 538–598. https://doi.org/10.1617/s11527-010-9650-4

Yokota, H., Rokugo, K., & Sakata, N. (2008). *JSCE-2008 Recommendations for design and construction of high performance fiber reinforced cement composites with multiple fine cracks (HPFRCC)*. Japan Society of Civil Engineers. https://doi.org/10.1016/j.dci.2010.01.003.

Yoo, D. Y., & Kim, M. J. (2019). High energy absorbent ultra-high-performance concrete with hybrid steel and polyethylene fibers. *Construction and Building Materials*, *209*, 354–363. https://doi.org/10.1016/j.conbuildmat.2019.03.096

Yu, R., Spiesz, P., & Brouwers, H. J. H. (2015). Development of ultra-high performance fibre reinforced concrete (UHPFRC): Towards an efficient utilization of binders and fibres. *Construction and Building Materials*, *79*, 273–282. https://doi.org/10.1016/j.conbuildmat.2015.01.050

Zhang, J., Zhao, Y., & Li, H. (2017). Experimental investigation and prediction of compressive strength of ultra-high performance concrete (UHPC) containing supplementary cementitious materials, Hindawi. *Advances in Materials Science and Engineering*, *2017*, 1–525. https://doi.org/10.1155/2017/4563164

Zhang, J., Zhao, Y., & Li, H. (2017). Experimental investigation and prediction of compressive strength of ultra-high performance concrete containing supplementary cementitious materials. Advances in Materials Science and Engineering, 2017, 4563164. https://doi.org/10.1155/2017/4563164